OPEN

# 7 Tesla and Beyond

## *Advanced Methods and Clinical Applications in Magnetic Resonance Imaging*

*Tanja Platt, PhD,* Mark E. Ladd, PhD,*†‡§ and Daniel Paech, MD, MSc||¶*

**Abstract:** Ultrahigh magnetic fields offer significantly higher signal-to-noise ratio, and several magnetic resonance applications additionally benefit from a higher contrast-to-noise ratio, with static magnetic field strengths of $B_0 \geq 7$ T currently being referred to as ultrahigh fields (UHFs). The advantages of UHF can be used to resolve structures more precisely or to visualize physiological/pathophysiological effects that would be difficult or even impossible to detect at lower field strengths. However, with these advantages also come challenges, such as inhomogeneities applying standard radiofrequency excitation techniques, higher energy deposition in the human body, and enhanced $B_0$ field inhomogeneities. The advantages but also the challenges of UHF as well as promising advanced methodological developments and clinical applications that particularly benefit from UHF are discussed in this review article.

**Key Words:** ultrahigh field, UHF, MRI, MRS, SWI, X-nuclei, $^{31}$P, $^{23}$Na, fMRI, CEST

(*Invest Radiol* 2021;56: 705–725)

Currently, clinical magnetic resonance (MR) examinations are mainly performed at static magnetic fields of 1.5 and 3 T. However, since the later 1990s, also many studies in humans have been performed at magnetic fields higher than 3 T.[1–7] In the period around the turn of the millennium, the first 2 ultrahigh field (UHF) MR systems for human MR applications were installed and applied in vivo,[1,5] with static magnetic field strengths of $B_0 \geq 7$ T currently being referred to as UHF. Based on the research work performed by these and subsequent research UHF systems, the first regulatory approval of a commercial 7 T MR system for clinical neuro and musculoskeletal (MSK) imaging as a medical device occurred in 2017.[8] In the meantime, a second manufacturer has also followed with the clearance of a 7 T MR scanner as a medical device. Until the first approval as a medical device, more than 70 UHF MR systems including several 9.4 T MR scanners were in operation as research devices. After approval, the number of UHF MR devices has increased noticeably, with a total number of UHF systems of approximately 100. The approval makes it possible not only to conduct basic research with these scanners, but also to perform clinical diagnosis. This simplifies studies including larger cohorts, because they can be carried out, for example, as part of clinical measurements with prior consent of the patient. In addition to the aforementioned MR systems with 7, 8, and 9.4 T, a first 10.5 T whole-body MR scanner is in operation,[9] and 11.7 T magnets for human MR imaging (MRI) are in the process of being launched at NeuroSpin CEA in Paris,[10] at the National Institutes of Health in Bethesda, and at the Gachon Medical University in Incheon. These systems are expected to provide very promising opportunities in future MR research.

In this review article, we discuss various promising MR methods and applications at $B_0 \geq 7$ T. Because of the large number of studies performed at UHF, we cannot guarantee completeness. The length of the individual text sections does not necessarily reflect the frequency of use or the readiness of the method for clinical application. Furthermore, the majority of the studies cited were not performed with product sequences and/or hardware but with custom-built hardware and/or sequences. Some of these techniques are therefore not directly available for immediate clinical use.

## PHYSICAL CHALLENGES AND ADVANTAGES OF ULTRAHIGH FIELD

In human MR applications, the measurement noise is sample-dominated in most cases, and for this case and for resonance frequencies at least up to approximately 64 MHz ($^1$H frequency at 1.5 T), a linear increase in signal-to-noise ratio (SNR) can be expected.[11] However, at UHF strengths ($B_0 \geq 7$ T) and thus higher proton resonance frequencies, even a higher increase in SNR has been observed for $^1$H MR applications in some cases, for example, an SNR increase proportional to $B_0$ raised to the power of 1.65 to 2.1.[9,12,13]

Thus, MRI at UHF provides a significant increase in the MR signal compared with 1.5 and 3 T, which are currently the standard field strengths in clinical MRI. This signal gain with increasing $B_0$ can be used on the one hand to achieve a higher spatial resolution in the same measurement time (see sections High-Resolution Morphological Magnetic Resonance Imaging and X-Nuclei Magnetic Resonance Spectroscopy and Magnetic Resonance Imaging) or to achieve similar image quality in a shorter measurement time, which also allows for a higher temporal resolution in dynamic MRI techniques.

In addition to SNR, the contrast-to-noise ratio (CNR) plays an important role in MRI techniques. Contrast generation in MRI is generally based on the interactions between nuclear spins and their variable environment, and there is a variety of contrasts that depend on diverse parameters (eg, $T_1$, $T_2$, …) that change differently with increasing $B_0$. For example, the longitudinal relaxation times $T_1$ of protons lengthen with $B_0$. As a result, time-of-flight (TOF) MR angiography and arterial spin labeling benefit from increased background suppression.[14–17] However, for applications that require, for example, full relaxation before the next excitation, longer $T_1$ times result in longer measurement times at higher fields.

Furthermore, higher magnetic fields provide increased susceptibility sensitivity,[17–19] which is of great advantage for susceptibility-weighted imaging (SWI) and quantitative susceptibility mapping (QSM) (see section High-Resolution Morphological Magnetic Resonance Imaging) but also for functional MRI (fMRI) (see section Functional Magnetic Resonance Imaging for Mapping Neuronal Activity). In other applications, however, this fact can lead to increased susceptibility artifacts including geometric distortions and signal dropouts in the images.

Received for publication May 5, 2021; and accepted for publication, after revision, August 7, 2021.

From the *Medical Physics in Radiology, German Cancer Research Center (DKFZ); †Faculty of Physics and Astronomy, and ‡Faculty of Medicine, University of Heidelberg, Heidelberg; §Erwin L. Hahn Institute for MRI, University of Duisburg-Essen, Essen; ||Division of Radiology, German Cancer Research Center (DKFZ), Heidelberg; and ¶Clinic for Neuroradiology, University of Bonn, Bonn, Germany.

Conflicts of interest and sources of funding: D.P. receives funding from the German Research Foundation (DFG; research grant project number 445704496). The other authors have no conflicts of interest and sources of funding to declare.

Correspondence to: Daniel Paech, MD, MSc, Division of Radiology, German Cancer Research Center (DKFZ), Im Neuenheimer Feld 280, 69120 Heidelberg, Baden-Württemberg, Germany. E-mail: d.paech@dkfz-heidelberg.de.



ISSN: 0020-9996/21/5611–0705
DOI: 10.1097/RLI.0000000000000820

For diffusion-weighted imaging (DWI), higher SNR at UHF also offers the possibility of increased resolution and/or high b-value acquisition.[20] However, increased $B_0$ and radiofrequency (RF) transmit field inhomogeneity, shorter $T_2$ relaxation, and higher specific absorption rate (SAR) levels are challenges that need to be addressed at UHF.[20] Despite short $T_2$, SNR gain at UHF has been demonstrated to be feasible with short echo times,[21] for example, by combining parallel imaging and partial Fourier acquisition.[22,23] Further echo time reduction can be achieved by reducing the field of view[24] and readout-segmented echo planar imaging.[25] Dielectric pads have been suggested for addressing RF transmit field inhomogeneity.[23] Such technical advances have paved the way for human applications of DWI at UHF.

In spectroscopic applications, a higher magnetic field strength leads to larger splitting of the resonance frequencies in the MR spectrum, which can be beneficial, for example, in $^1$H MR spectroscopy (MRS; see section Proton Magnetic Resonance Spectroscopy and subsection Phosphorus-31 Magnetic Resonance Spectroscopy) or chemical exchange saturation transfer (CEST; see section Chemical Exchange-Sensitive Magnetic Resonance Imaging) acquisition techniques.[26–28]

## Radiofrequency Characteristics of $^1$H at Ultrahigh Field: Issues With Field Inhomogeneity

With increasing field strength and thus increasing resonance frequency, the wavelength for $^1$H RF excitation in humans approaches the size of the head, body part, or body, causing standing wave effects. For $^1$H MR applications at approximately 300 MHz or higher for $B_0$ = 7 T and beyond, strong inhomogeneities in the transmit field ($B_1^+$) and in the receive field ($B_1^-$) can occur, which can lead to cancellations in the MR images, impaired contrasts, and regional peaks in the SAR distribution.[17,29]

Thus, coil designs that are used at lower $B_0$, such as standard surface and birdcage coils, can therefore exhibit disadvantageous behavior at UHF for the excitation of medium to large excitation volumes.[4,30] In body MR applications, birdcage coils are practically not applicable because of the enormous inhomogeneities in $B_1^+$ and $B_1^-$. Therefore, the manufacturers of MR systems do not offer an integrated body coil behind the bore liner of the magnet, and also so far no other $^1$H RF body coil for MRI of the human torso. Dedicated coils for excitation (transmission) and detection (reception of the spin signal) are therefore required for each specific body region.

To deal with the challenges of inhomogeneous RF fields and enable $^1$H MRI, even in larger body regions, excitation hardware and techniques have been further developed during the last decades, using multiple transmit RF coil elements and multiple transmit channels. With so-called $B_1^+$ shimming or static RF shimming, a transmit coil array is driven with a single RF waveform, and the phases in the coil elements are independently adjusted. This technique was a first step to improve the $B_1^+$ field homogeneity, and it achieves homogeneous excitation in small regions of interest (ROIs) such as the prostate or a specific brain region. In larger ROIs, the time-interleaved acquisition of modes method is a valuable extension[31]: 2 (or more) measurements with identical parameters but with different $B_1^+$ shim weights are acquired. The acquired data are merged, and a single image is reconstructed with reduced contrast variations.

With dynamically applied $B_1^+$ shimming, it is possible to switch to another shim after an RF pulse.[32] This allows RF pulses with different static shims to be played out, which can be used if the pulses are to excite different ROIs, for example, for saturation, inversion, and so on.

Dynamic or full parallel transmission techniques (dynamic/full pTx) exploit the amplitudes and phases of the multiple transmit channels as additional degrees of freedom to optimize the $B_1^+$ field distribution or to tailor the spin magnetization in an ROI.[33] For pTx, typically not only all RF pulse shapes are optimized individually for each transmit coil element, but also the gradient trajectories are optimized. In addition, pTx techniques require 2-dimensional (2D) or 3-dimensional (3D) $B_1^+$ field maps of each individual channel, which are a prerequisite for the determination of the pulse shapes and gradient trajectories. In early pTx implementations, the necessary preparation steps were complex and time-consuming. With the latest 7 T MR system, $B_1^+$ shimming (static RF shimming) can be performed in a short time that does not significantly prolong the clinical workflow. However, the preparation steps for dynamic pTx are still time-consuming and can only be performed in research mode.

To avoid these calibrations before each measurement in vivo, so-called universal pulses were developed, which were optimized based on the $B_1^+$ field maps of 6 subjects in the initial implementation. The resulting pulses can then be applied in other subjects without the need for calibration. This method significantly reduces the time needed before the actual measurement and thus offers great potential for future clinical application.[34] A recent approach combines universal pTx pulses and a fast subject-specific optimization for human brain MRI. This enables the calculation of individually optimized pTx pulses within a maximum of 15 seconds.[35]

In general, dynamic pTx can be applied for global, slice-selective, or slab-selective excitation and for 2D or 3D selective excitation. A detailed overview on pTx techniques is given, for example, by Padormo et al.[33] In addition to inhomogeneities in $B_1^+$ and $B_1^-$, cancellations and hot spots can also occur in the local SAR distribution, which depends on the RF electric field pattern. This must be considered during the safety assessment; a detailed overview of this topic can be found in the review by Fiedler et al.[29] Therefore, there are currently hardly any commercial pTx body coils with regulatory approval available. Thus, a product pTx body coil, including safety aspects and SAR monitoring by the vendor, would greatly facilitate access to the torso at UHF.

## Physical Characteristics of Nonproton MRS and MRI at UHF

Magnetic resonance data from nonproton nuclei with a nonvanishing nuclear spin such as phosphorus-31 ($^{31}$P) and sodium-23 ($^{23}$Na) contain information about metabolic and functional processes that is highly valuable, as these nuclei are directly involved in many biological processes. In this section, the general physical properties of nonproton MRS and MRI at UHF are briefly discussed. A review of the detailed characteristics of each discussed nucleus as well as the relevant methods and clinical applications are given in the section X-Nuclei Magnetic Resonance Spectroscopy and Magnetic Resonance Imaging.

As with proton applications, nonproton MRS/MRI benefits from the increase in MR signal with $B_0$. Figure 1 shows that, at $B_0$ = 7 T, $^{23}$Na MRI in the brain becomes achievable in clinically feasible measurement times.

Spectroscopic nonproton applications, in common with $^1$H MRS, additionally profit from the larger splitting of resonance frequencies in the MR spectrum. For example, at 7 T, it is possible to distinguish 2 resonances of inorganic phosphate in the $^{31}$P MR spectrum, the intracellular $P_i^{in}$ and the extracellular $P_i^{ex}$ peaks.[37,38]

Because of the fact that the Larmor frequency is nucleus-specific and depends on $B_0$, each combination of X-nucleus and field strength $B_0$ results in an individual resonance frequency (see section X-Nuclei Magnetic Resonance Spectroscopy and Magnetic Resonance Imaging). For a majority of X-nuclei, the resonance frequency at $B_0$ = 7 T or $B_0$ = 9.4 T is below 130 MHz (approximately $^1$H at $B_0$ = 3 T or $^{31}$P at $B_0$ = 7 T) and thus much lower than 300 MHz. In contrast to $^1$H MRI/MRS at $B_0 \geq$ 7 T, standing wave effects in the $B_1^+$ field are negligible or manageable for X-nuclei MRI up to 130 MHz,[36] and standard RF coil designs can be suitable: (1) surface coils provide high $B_1^+$ and $B_1^-$ efficiency near the coil, which is advantageous for MRS, but the field distributions are inhomogeneous; (2) birdcage coils provide homogeneous field distributions over a large field of view, which is advantageous for concentration quantification of, for example, $^{23}$Na and oxygen-17 ($^{17}$O), but with the disadvantage of lower sensitivity.

However, for fluorine-19 ($^{19}$F) spin excitation, the resonance frequency is roughly 280 MHz at $B_0$ = 7 T, and as with protons at $B_0 \geq$ 7 T, strong field inhomogeneities can occur during excitation in large

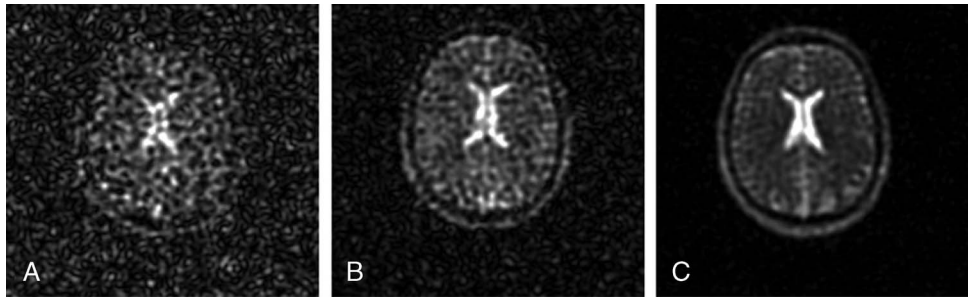


**FIGURE 1.** Sodium ($^{23}$Na) MRI at 1.5 (A), 3 (B), and 7 T (C). Images show that the SNR increases markedly with $B_0$. Sequence parameters: TE (1.5 and 3 T), 0.2 milliseconds; TE (7 T), 0.5 milliseconds; TR, 50 milliseconds; flip angle α, 77 degrees; nominal spatial resolution, 4 mm$^3$; acquisition time, 10 minutes 50 seconds. Reused with permission from John Wiley & Sons, Kraff et al.[36]

samples. Therefore, dedicated excitation hardware and techniques are also required for $^{19}$F MRS/MRI in large samples at $B_0 \geq 7$ T.

Magnetic resonance systems with $B_0 = 7$ T and higher do not have $^1$H body coils installed because of the aforementioned problems with transmit homogeneity. Therefore, local dual-tuned RF coils that support $^1$H MRS/MRI in addition to X-nuclei MRS/MRI can enable or simplify standard $B_0$ shimming as well as anatomical localization and coregistration. For a detailed discussion on nonproton MRS/MRI at UHF, please refer to the section X-Nuclei Magnetic Resonance Spectroscopy and Magnetic Resonance Imaging.

## HIGH-RESOLUTION MORPHOLOGICAL MAGNETIC RESONANCE IMAGING

High-resolution proton MRI is still the major field for clinical applications at UHF. Static field strengths of 7 T provide higher SNR and in several applications higher CNR in comparison to MRI at lower field strengths that translates into increased resolution and improved differentiation among different tissue types. However, high-resolution MRI is consequently more prone to present motion artifacts, and particularly for inpatients and in the emergency department, motion is a common cause of MR image degradation.[39] Various prospective and retrospective motion correction methods are available that have been developed at lower field strengths.[40] At 7 T, ultrahigh-resolution images can be achieved applying motion correction.[41–43] The following sections provide an overview of important clinical applications of high-resolution imaging using UHF MRI.

### Neuroradiology

There is a fast-growing body of evidence that particularly in the field of neuroradiology UHF MRI has the potential to aid diagnostics and clinical decision making. The increased resolution at UHF MRI improves depiction of anatomical substructures.[44–47] For instance, visualization of cranial nerves has been demonstrated at 7 T using magnetization-prepared rapid acquisition gradient echo (MPRAGE) and MP2RAGE MRI that could help diagnosis of cranial nerve disorders.[48]

High-resolution morphological imaging has also been demonstrated feasible for the complex anatomical structures of the brain stem, including nonquantitative techniques (eg, $T_2$- and proton density–weighted imaging) and quantitative approaches, such as QSM, relaxation measurements ($R_2$*, $R_1$), and diffusion tensor imaging (Fig. 2).[49]

Generally, methods based on magnetic susceptibility MRI benefit strongly from strong magnetic fields.[50] Postprocessed phase images sensitive to magnetic susceptibility enhance the gray/white matter contrast.[51] Susceptibility-weighted imaging can help to depict cerebral cavernous malformations[52] and to further characterize white matter lesions.[53] Furthermore, MR venograms using deoxyhemoglobin (as an intrinsic contrast agent) can be obtained with very detailed information.[54] Magnetic resonance angiography (MRA) with 3D arterial TOF at UHF improves the visualization of small intracranial vessels and has the potential to better characterize vessel walls.[55,56] Seven Tesla MRI has also been demonstrated to enhance the depiction of small cerebral aneurysms and arteriovenous malformations (AVMs),[57,58] enabling the detection of microaneurysms with diameters ≤1 mm.[59] Dynamic information about the blood flow patterns within the AVM, for instance assessable via phase-contrast 4D flow MRI,[60,61] may further improve endovascular or surgical treatment planning in such diseases.

Magnetic resonance imaging is the most sensitive imaging technique to detect acute brain infarctions in patients with stroke.[62] Minor ischemic infarcts were found by Novak and colleagues[63] using $T_2$-weighted gradient echo (GRE) and rapid acquisition with relaxation enhancement images at 8 T that were not detectable on routine MRI at 1.5 T. Moreover, cortical microinfarcts have been described using 7 T magnetization transfer (MT), which is only possible to a limited extent at 3 T.[44,64–66]

In patients with brain cancer, MRI represents a cornerstone in diagnosis, treatment planning, and during follow-up.[67] Higher spatial resolution at 7 T could help to better differentiate infiltrative tumor from neighboring tissues[68,69] or to reduce the administered contrast agent dose because of increased CNR.[70] Furthermore, therapy-related changes in normal-appearing brain tissue may be better distinguished from residual or relapsing neoplasm.[71] Neoangiogenesis of tumors can be visualized using 7 T TOF MRA, which could potentially be used to monitor response to antiangiogenic therapies.[72]

In patients with multiple sclerosis (MS), better visualization of white matter lesions as well as the depiction of a central vein ("central vein sign") and iron deposits within MS lesions have been described (Fig. 3).[46,73–75] Although several studies reported more lesions being detected at UHF compared with clinical field strength (1.5 T or 3 T), the literature is inconsistent regarding the diagnostic confidence for the diagnosis of MS using 7 T MRI.[46] Recent studies, however, reported growing evidence that 7 T has the potential to improve MS diagnosis.[76]

In neurodegenerative diseases, more precise volumetric assessments of the hippocampal subfields and the entorhinal cortex can be performed at 7 T. Such investigations showed volume reductions in patients with Alzheimer disease (AD) in all hippocampal subfields and the entorhinal cortex compared with healthy controls and patients with mild cognitive impairment (MCI).[77,78] Microbleeds and white matter lesions are associated with vascular dementia. For this type of dementia, UHF MRI has been reported to yield improved sensitivity for an early diagnosis.[79,80]

Loss of dopaminergic neurotransmission of the substantia nigra and tegmental area is associated with Parkinson disease (PD) and neuropsychiatric disorders. $T_2$*-weighted MRI and SWI acquired at UHF have been shown to allow better visualization of the substantia nigra and its inner organization,[81–83] which could aid target identification for deep brain stimulation.[84,85]

In the neurologic assessment of patients with epilepsy, MRI is a highly sensitive modality for the identification of epileptogenic foci.[86]

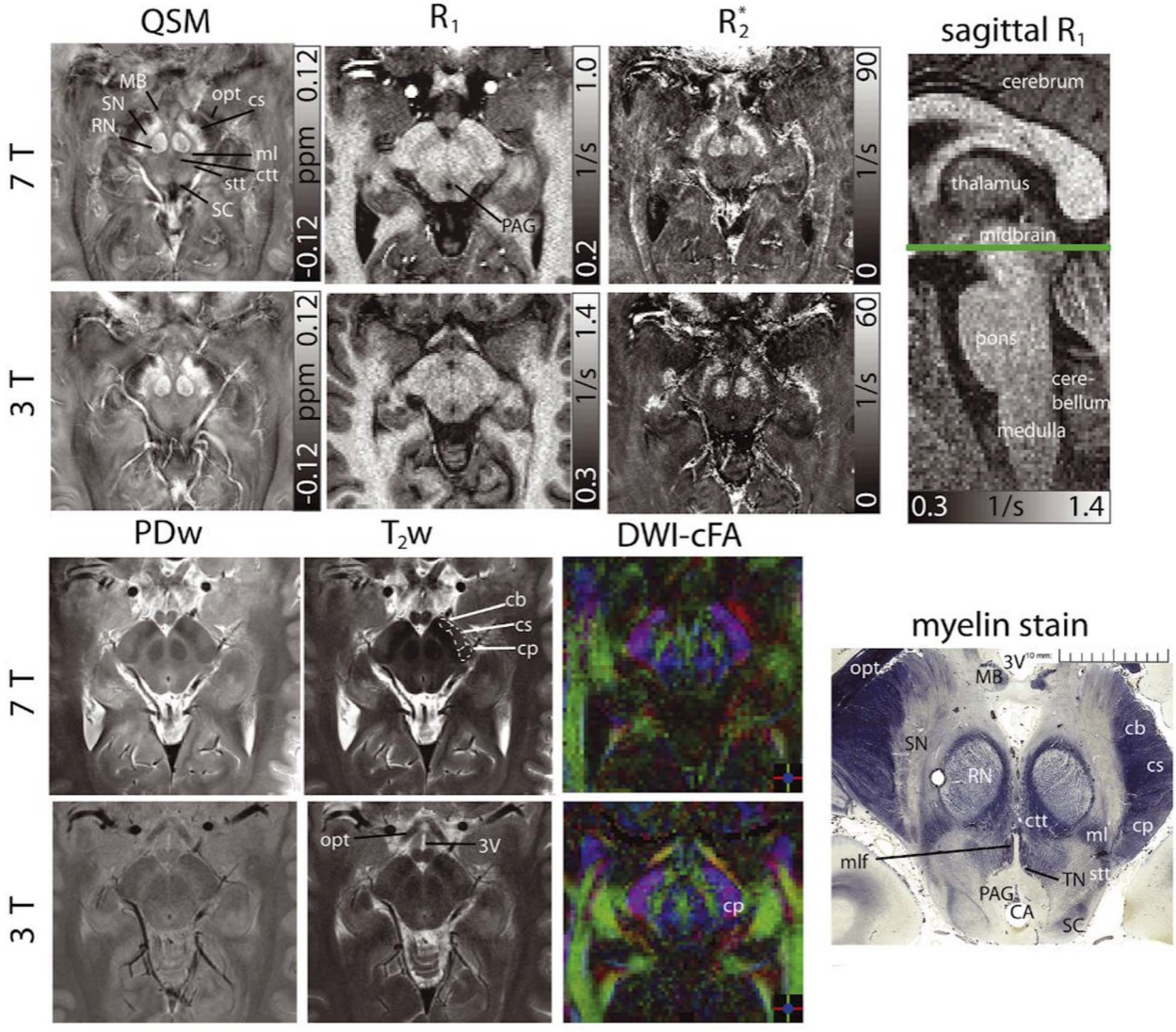


**FIGURE 2.** Susceptibility, $R_1$, $R_2$* maps, proton density-, $T_2$-weighted images, and color-coded diffusion anisotropy maps (left to right and top to bottom) of the same transverse slice in one healthy volunteer showing detailed anatomical substructures in the midbrain at 7 T and 3 T. A sagittal $R_1$ image indicates the slice location. Histologic myelin stain additionally shown for anatomical correlation (myelin stain reproduced from http://www.brains.rad.msu.edu and http://brainmuseum.org, supported by the US National Science Foundation). The cerebral aqueduct (CA), crus cerebri (corticobulbar fibers [cb], corticospinal fibers [cs], corticopontine fibers [cp]), the central tegmental tract (ctt), the mammillary body (MB), the medial lemniscus (ml), the medial longitudinal fasciculus (mlf), the optic tract (opt), the periaqueductal gray (PAG), the red nuclei (RN), the spinothalamic tract (stt), the substantia nigra (SN), the superiorcolliculus (SC), and the third ventricle (3 V) are indicated. The trochlear nuclei (TN) can only be clearly delineated in the histology stain. For better clarity, bilateral structures are only indicated monolaterally and at 7 T images. Reused with permission from John Wiley & Sons, Straub et al.[49]

The gain in SNR and CNR at $B_0 \geq 7$ T has been shown to improve the detection of possible epileptogenic zones, for example, focal cortical dysplasia, compared with MR scans at 3 T or 1.5 T.[87–92] Furthermore, better soft tissue contrast of the hippocampal architecture was achieved in patients with mesial temporal sclerosis at UHF MRI.[89] Investigations of hippocampal and temporal lobe volumes at 7 T revealed lateralization effects in patients with temporal lobe epilepsy.[93] The 7 T Epilepsy Task Force—an international group representing twenty-one 7 T MRI centers with experience from scanning over 2000 patients with epilepsy—has outlined the potential diagnostic value of 7 T MRI and provided guidance for appropriate clinical indications, patient selection, and radiologic guidelines for UHF MRI in patients with epilepsy.[92] The clinical evidence of the added value of 7 T MRI for the management of patients with epilepsy is far beyond the current status of applications in other diseases. The 7 T Epilepsy Task Force could therefore serve as a role model for other fields, currently being investigated with 7 T.

## Musculoskeletal Magnetic Resonance Imaging

Besides recent approval for clinical applications in neuroradiology, 7 T scanners have been approved for selected MSK applications in both the United States and the European Union.

High-resolution spin echo and GRE-based pulse sequences have been applied at 7 T to assess trabecular bone microarchitecture with improved visualization of anatomical substructures and quantitative measures of both bone volume fraction and marrow volume fraction (Fig. 4).[95–98] High spatial resolution is mandatory to visualize trabecular

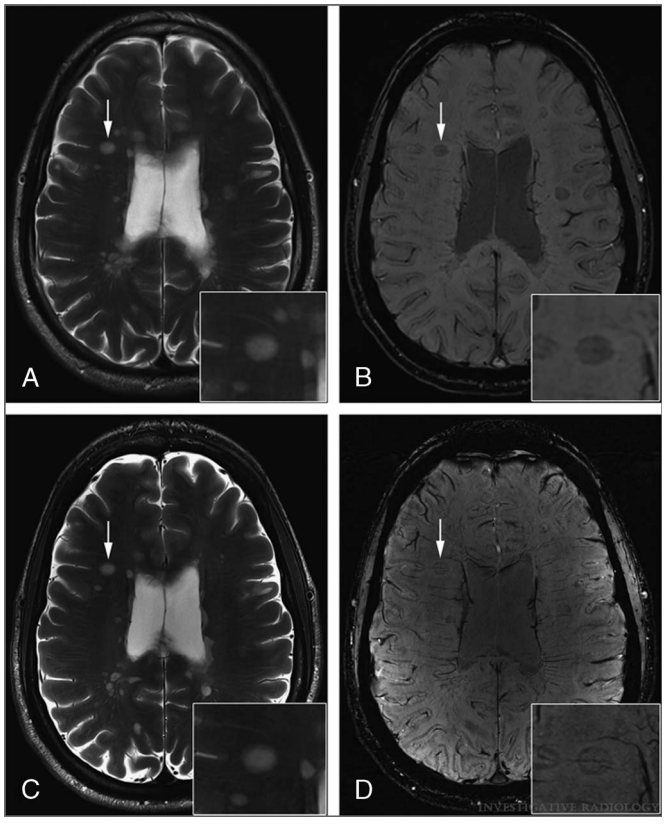


**FIGURE 3.** Axial $T_2$-weighted images of an MS patient acquired at 3 T (A) and 7 T (C) and corresponding axial SWI scans acquired at 3 T (B) and 7 T (D). Note the central vessels and iron deposits (rims) within MS lesions in SWI scans (B and D, white arrows). In $T_2$-weighted images, central vessels are challenging to depict (A and C, white arrows). Reused with permission from Wolters Kluwer Health, Inc, Springer et al.[46]

bone morphology, because the average diameter of the individual trabeculae is on the order of 100 to 150 μm.[94]

For ankle MRI, Juras et al[99] showed that both SNR (3D GRE) and CNR (2D turbo spin echo [TSE] and 2D GRE) significantly increase from 3 T to 7 T and therefore inferred a substantial diagnostic benefit using UHF. The diagnostic performance of 7 T versus 3 T in the detection of joint pathologies has been assessed by Springer et al[100] in 40 patients with knee pain. Besides significant gains in SNR (2D $T_2$ TSE, 2D TSE proton density, 3D dual-echo steady-state $T_2$), 7 T improved overall diagnostic confidence (semiquantitative assessment), particularly for fine structures in joints, as well as for subtle lesions in bone, menisci, and cartilage.[100] Furthermore, intermediate-weighted, fat-suppressed, fluid-attenuated inversion recovery MRI of the knee at 7 T has been demonstrated as a potential nonenhanced MRI method to visualize synovial inflammation in patients with psoriatic or rheumatoid arthritis.[101]

$T_2$ and $T_2$* mapping at 7 T have been applied to assess cartilage collagen matrix integrity and have been shown to positively correlate with water content.[102,103] Because of the increased resolution at UHF, both $T_2$ and $T_2$* MRI were less prone to partial volume effects than similar approaches at 3 T.[104] In addition, in vivo $T_1$-weighted delayed gadolinium-enhanced MRI of cartilage (dGEMRIC) has been demonstrated to be feasible in healthy and reparative articular cartilage at 7 T MRI.[105] Zonal assessment of deep and superficial cartilage by means of dGEMRIC, $T_2$, and $T_2$* mapping may aid differentiation of healthy and affected articular cartilage in the future.[105]

Diffusion tensor imaging has also been applied to assess cartilage matrix integrity through fractional anisotropy and the apparent diffusion coefficient. Raya et al[106] reported that both fractional anisotropy and apparent diffusion coefficient allowed distinguishing between healthy cartilage and cartilage affected by osteoarthritis.

$T_1\rho$ imaging, which describes the relaxation of magnetization in the rotating frame, has been used to study proteoglycan content in cartilage. Magnetic resonance imaging at 7 T benefitted from increased SNR and chemical shifts compared with 3 T MRI, resulting in higher sensitivity to molecular changes at the same resolution.[107]

Wei and colleagues[108] investigated knee cartilage pathologies with SWI at 7 T. They found that the arrangement of the collagen fibrils

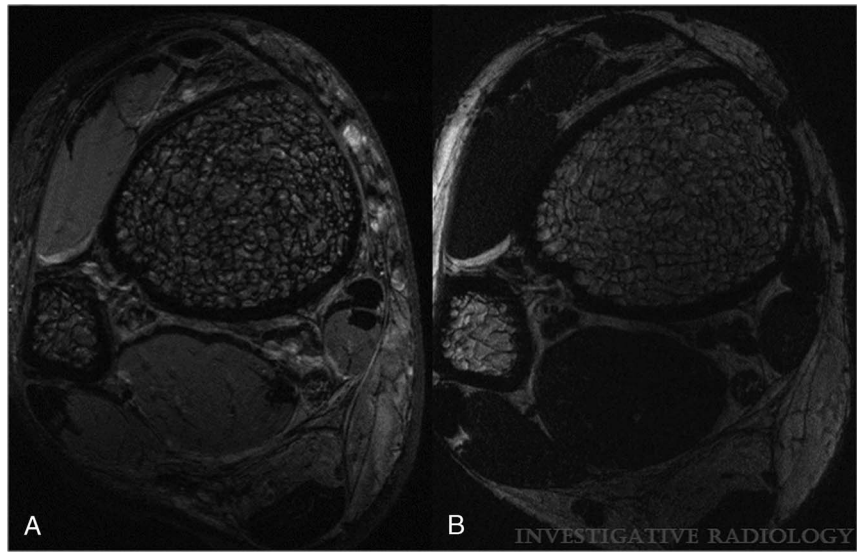


**FIGURE 4.** Magnetic resonance images of the distal tibia acquired in vivo with FIESTA-C at 7 T (A) and 3 T (B) are depicted. The enhanced visualization of trabecular bone structure at 7 T is well demonstrated by these images. Please note that, although the same sequence is used, chemical shift and susceptibility artifacts are enhanced at 7 T, shown by thicker appearing trabeculae and at the muscle/fat interface. Also, the image contrast and signal of muscle and fat are different at 7 T and 3 T. Reused with permission from Wolters Kluwer Health, Inc, Krug et al.[94]

is the most dominant source of magnetic susceptibility anisotropy. Moreover, feasibility of QSM to characterize magnetic susceptibility properties of tissues in the knee joint has been demonstrated.[108] The authors inferred that QSM may be useful for evaluating the status of knee diseases, such as meniscal tears and cartilage disease, because of its sensitivity to collagen damage or degeneration.

Preliminary results of human spine MRI have been reported using multichannel transmit/receive phased array RF coils, demonstrating the feasibility of spine MRI at UHF.[109,110] Ultrahigh field human spine RF transceiver coil arrays face technical challenges in achieving large imaging coverage with sufficient $B_1$ penetration and sensitivity and in attaining robust decoupling among coil elements.[109] Comparisons of the diagnostic performance in lumbar spine MRI at 7 T versus 1.5/3 T could not prove superior imaging quality, so far precluding routine clinical use.[111] However, recent developments of novel coil technology (ie, 16-channel receive array as an add-on to multichannel transmit/receive RF coil configurations) have been demonstrated to increase SNR, lower g-factors, and thus improve 7 T spine MRI at 7 T.[112]

Different groups have demonstrated the feasibility of high-resolution cervical spinal cord MRI at 7 T, including multiparametric quantitative MRI,[113] diffusion tensor imaging,[114] and dynamic susceptibility contrast imaging.[115] Three-dimensional dual-echo steady-state MRI at 7 T has been shown to allow precise assessment of the microanatomy of intraspinal cervical nerve roots.[116]

## Abdominal and Thoracic Magnetic Resonance Imaging

Although the benefits of increasing field strength for neuroradiological and MSK applications have already been demonstrated in many cases, only few studies have so far investigated the potential of 7 T MRI for abdominal and thoracic MRI. Continuing developments in RF body coil technology and $B_1^+$ shimming encourage the further exploration of UHF MRI in this area. Laader et al[117] demonstrated that 7 T MRI showed partially comparable as well as both improved and inferior MRI results in the abdomen compared with lower field strengths, with substantial differences for $T_1$- and $T_2$-weighted MRI. Higher SNR and CNR were observed in multiple abdominal organs, potentially enabling detection of small pathologies that may be missed at lower field strength (Fig. 5).[117]

Umutlu et al[118] demonstrated that 7 T MRI of the kidneys is feasible providing good overall image quality, particularly for $T_1$-weighted GRE MRI. $T_2$-weighted TSE and TrueFISP MRI were limited at 7 T because of artifacts and SAR restrictions. Fischer et al[119] demonstrated feasibility of contrast-enhanced MR cholangiopancreatography at UHF. Results were evaluated as equivalent but not superior in comparison to 3 T MR cholangiopancreatography, that is, because of residual $B_1$ field inhomogeneities.[119]

Prostate MRI in clinical routine mainly relies on $T_2$-weighted MRI and DWI (± dynamic contrast-enhanced MRI). High-resolution $T_2$-weighted TSE MRI of the prostate for improved delineation of prostate anatomy has been demonstrated and applied in patients with prostate cancer using an 8-channel transmit/receive RF body array.[120,121] Cancer lesions in both peripheral zone and transition zone were delineable at 7 T.[121] Multichannel endorectal coil have been proposed for use in combination with an external surface array for high-resolution anatomical and functional studies of the prostate at 7 T.[122] For the assessment of pelvic lymph nodes (eg, for the evaluation of metastatic disease), feasibility of high-resolution USPIO-enhanced MRI has been demonstrated at 7 T.[123]

Bilateral RF breast coils are mandatory to achieve high spatial resolution and high contrast in breast MRI applications at 7 T.[124] In patients with breast cancer, dynamic contrast-enhanced breast MRI,[125] DWI,[126] and multiparametric approaches[127,128] have been proven feasible in clinical settings with the potential to improve diagnostic accuracy.

Technical feasibility of 7 T cardiac MRI has been demonstrated using steady-state free precession and fast gradient echo sequences for cardiac cine MRI.[129–132] Generally, residual $B_1$ field inhomogeneities and the consequent need for further development of RF coils and pTX optimization are challenges that need to be addressed by researchers and manufacturers. Schmitter et al[133] combined pTX and simultaneous excitation of multiple slices (from a limited number of slices during breath-hold) to

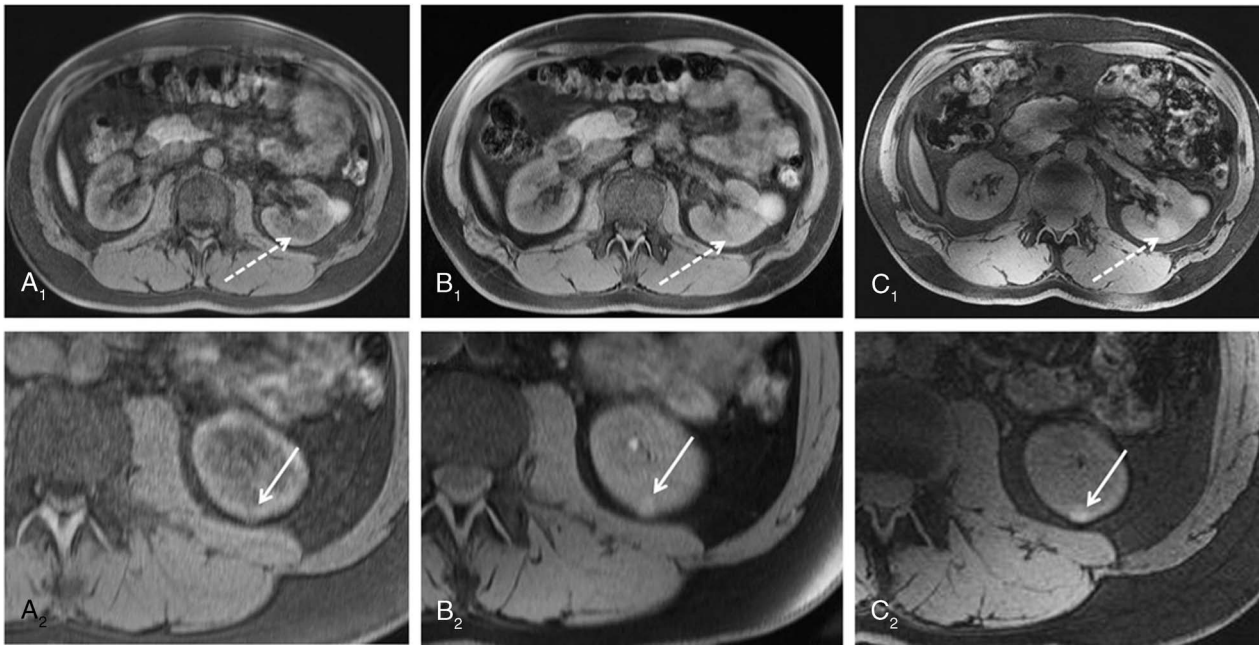


**FIGURE 5.** Three-dimensional VIBE MRI at 1.5 T (A), 3 T (B), and 7 T (C) in the same subject. Seven Tesla 3D VIBE MRI demonstrated diagnostic potential by means of pathology detection, as it revealed a second hemorrhaged renal cyst (dashed arrow $C_1$) not displayed at lower field strengths. In the second row, arrows show a further very small renal cyst in the same subject, which is also best visible at 7 T ($C_2$). Reproduced with permission, open access, Laader et al.[117]

reduce contrast heterogeneity while allowing larger slice coverage in cardiac MRI at 7 T.

## X-NUCLEI MAGNETIC RESONANCE SPECTROSCOPY AND MAGNETIC RESONANCE IMAGING

Besides protons, other nuclei with a nonvanishing nuclear spin can also be detected by MRS/MRI. Magnetic resonance applications of these nuclei are termed X-nuclei, nonproton, or multinuclear MRI/MRS applications. General physical properties of nonproton MRS and MRI at UHF are briefly described in the section Physical Characteristics of Nonproton MRS and MRI at UHF. In the following subsections, the nucleus-specific characteristics, methods, and clinical applications are described.

In general, the strength of these X-nuclei MR methods is that they are able to provide information that cannot be obtained with conventional proton MRI; for example, they directly provide insights into energy substrates and pH,[134] ion balance,[135] and cerebral oxygen turnover.[136]

However, low sensitivities and/or low in vivo concentrations of X-nuclei, along with other nuclei-specific properties (see following sections), pose challenges for X-nuclei MRI/MRS. Consequences are generally long measurement times, low spatial resolutions on the order of several $mm^3$, and partial volume effects. A summary of general MR properties for different X-nuclei is given in Table 1. The MR signal $S$ depends on the nucleus-specific quantities spin $I$, gyromagnetic ratio $\gamma$, natural abundance $\alpha$, and on the in vivo concentration $c$ as follows.

$$S \sim I\,(I+1)\cdot\gamma^3\cdot\alpha\cdot c \qquad \text{(Equation 1)}$$

Unlike proton MRI/MRS, X-nuclei applications have thus far not been established clinically at conventional field strengths of 1.5 T or 3 T, so there is a fundamental opportunity to translate X-nuclei MRI/MRS into clinical use at UHF. At least one manufacturer has secured regulatory approval for both $^{31}$P spectroscopy/spectroscopic imaging for the whole body excluding the head and $^{23}$Na imaging of the head at 7 T.[138] However, X-nuclei MRS and MRI techniques are currently applied almost exclusively in research studies.

### Phosphorus-31 Magnetic Resonance Spectroscopy

Phosphorous ($^{31}$P) is a spin-1/2 nucleus, and thus, $^{31}$P MRS enables the detection of energy substrates such as phosphocreatine (PCr), adenosine triphosphate (ATP), adenosine diphosphate, and inorganic phosphate ($P_i$). In addition, the resonances of phosphocholine, phosphoethanolamine, glycerophosphocholine, and glycerophosphoethanolamine provide insights into the cellular and mitochondrial membranes.[139] Consequently, valuable information about the energy and membrane metabolism can be obtained from a $^{31}$P spectrum.

Because of the increasing influence of chemical shift anisotropy on the relaxation mechanisms, a decrease in phosphorous $T_1$ relaxation time with increasing field strength was observed in the human calf for 7 T versus 3 T, which can allow shorter measurement times or additional SNR per unit time at higher field strengths.[140] In addition, the nuclear Overhauser effect (NOE) and decoupling can be used to increase the SNR and to simplify the spectrum. However, UHFs complicate these approaches because of the required high-power deposition, and therefore SAR issues, as well as the inhomogeneities in the $^1$H $B_1^+$ field.[141]

Furthermore, the absolute pH value can be calculated from the distance between the PCr resonance and the $P_i$ resonance in the $^{31}$P spectrum, which enables mapping of the pH value.[142,143] In recent years, it has been shown that, with the higher spectral resolution at $B_0 \geq 7$ T, it is possible to detect 2 $P_i$ signals: the intracellular $P_i^{in}$ and the extracellular $P_i^{ex}$.[37,38] Although quantification of extracellular pH is challenging because of the low SNR in vivo, recent studies have shown that determination of both intracellular and extracellular pH in the human brain is feasible using $^{31}$P MRS at 7 T.[144]

So far, several studies have been performed in small cohorts in the brain as well as in the calf muscle,[139,145] where it was demonstrated, for example, that UHF $^{31}$P MRS enables the investigation of the creatine kinase rate, ATP synthesis rate, and nicotinamide adenine nucleotide ($NAD^+$, NADH).[38,146–149]

The development of $^{31}$P volume coils[150–152] or dedicated $^{31}$P coils for specific body regions[153–155] for 7 T $^{31}$P MR applications enables valuable insights into body regions beyond the head, with increased SNR and spectroscopic resolution. A first human cardiac $^{31}$P spectrum at 7 T[156] showed that SNR of every peak increases compared with 3 T, for example, the SNR of PCr increased by factor of 2.8.

However, up to now, $^{31}$P MR studies in patients have mainly been performed at field strengths below 7 T. This may be because of the limited availability of UHF scanners, which may change with the increase in the number of 7 T MR systems and with the distribution of 7 T MR systems as a medical device enabling $^{31}$P MRS/MR spectroscopic imaging (MRSI) for the whole body excluding the head.[138]

#### Neuroradiology

A large number of studies have dealt with $^{31}$P MRS in neurological diseases, for example, in PD, where mitochondrial dysfunction and alterations of membrane phospholipid metabolism were observed at 1.5 and 3 T.[157–161] However, metabolic changes in early and mildly affected PD patients could not be detected reliably at 3 T.[162] Abnormal phosphate

**TABLE 1.** Overview of the Nucleus-Specific Properties of Commonly Used X-Nuclei in MRI/MRS, Including the Spin I, the Gyromagnetic Ratio $\gamma$, and the Natural Abundance α

| Nucleus | I, $\hbar$ | $\frac{\gamma}{2\pi}$, MHz/T | α, % | Relative Sensitivity, % | Relative Signal |
|---|---|---|---|---|---|
| $^1$H | 1/2 | 42.6 | 99.99 | 100 | 1 |
| $^2$H | 1 | 6.5 | 0.015 | 0.0001 | $10^{-6}$ |
| $^{13}$C | 1/2 | 10.7 | 1.07 | 0.017 | $10^{-5}$ |
| $^{17}$O | 5/2 | −5.8 | 0.04 | 0.0012 | $10^{-5}$ |
| $^{19}$F | 1/2 | 40.1 | 100 | 83.4 | $10^{-5}$ |
| $^{23}$Na | 3/2 | 11.3 | 100 | 9.25 | $10^{-5}$–$10^{-4}$ |
| $^{31}$P | 1/2 | 17.3 | 100 | 6.63 | $10^{-6}$ |
| $^{35}$Cl | 3/2 | 4.2 | 75.78 | 0.356 | $10^{-5}$ |
| $^{39}$K | 3/2 | 2.0 | 93.26 | 0.0473 | $10^{-5}$ |

The relative sensitivity of the X-nuclei compared with conventional proton sensitivity is given as well as the relative sensitivity strength (see Equation 1), where the in vivo concentration was additionally accounted for. Table modified from Niesporek et al.[137]

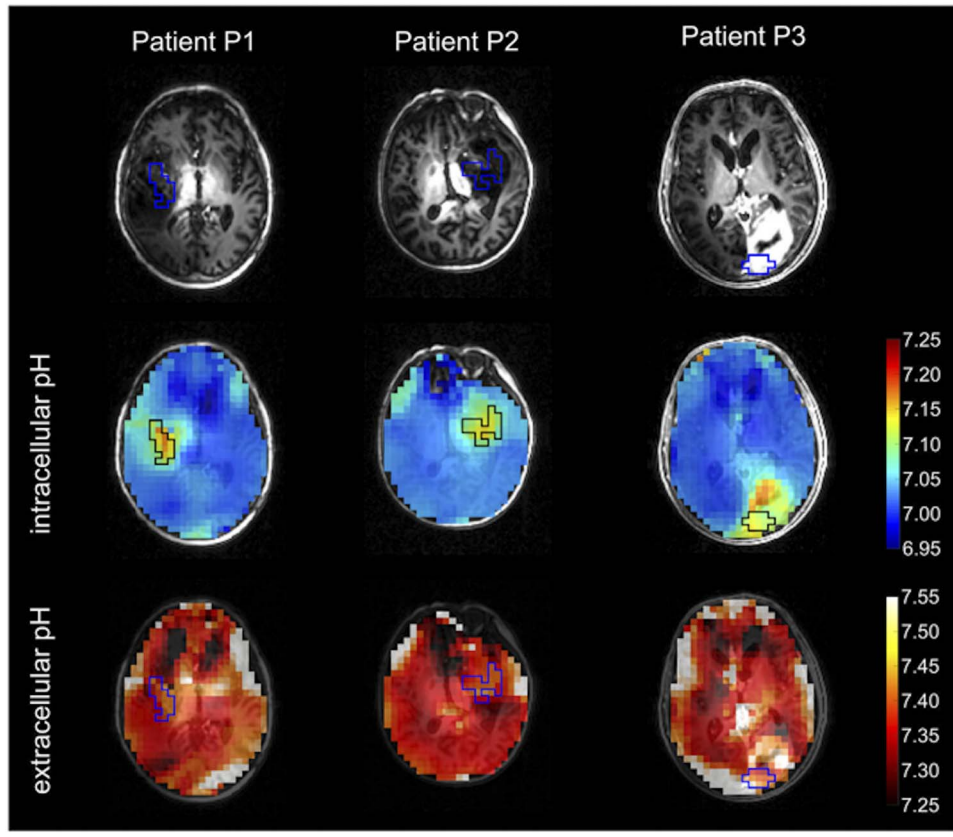


**FIGURE 6.** Axial intracellular and extracellular pH maps in 3 patients with glioma merged with nonenhanced $T_1$-weighted MPRAGE (black/blue boxes: manually segmented tumor ROIs within the solid tumor compartment). Reused with permission from John Wiley & Sons, Korzowski et al.[144]

metabolite and ion concentrations were detected in multisystemic atrophy via $^{31}$P MRS; thus, $^{31}$P MR applications might enable the differentiation between multisystemic atrophy and PD.[163] Moreover, in mild AD, increased PCr and pH were observed,[164] and in patients with epilepsy, alterations in mitochondrial function were detected via $^{31}$P MRS.[165,166]

The higher SNR and the higher spectral resolution at UHF offer great potential for investigating neurological diseases via $^{31}$P MR applications. For example, abnormal energy metabolism in cortical brain region of PD patients was demonstrated with $^{31}$P MRS at 7 T.[167]

At 9.4 T, high-resolution pH mapping with a nominal voxel size of 15 mm$^3$ was performed in the healthy human brain as well as in patients with brain tumors.[134] Recently, the feasibility of volumetric mapping of intracellular as well as extracellular pH in patients with brain tumors was demonstrated at 7 T (Fig. 6), offering the potential to provide new insights into the pH heterogeneity of different tissues, especially in tumor tissues.[144]

### Body Applications

$^{31}$P MRS in the liver has been applied in a broad spectrum of pathologies, including viral and alcoholic liver disease, nonalcoholic fatty liver, cirrhosis, diabetes, insulin resistance, and liver metastases at 1.5 and 3 T.[145] The feasibility of $^{31}$P MRS in the human liver was also demonstrated at 7 T,[168–170] and patients with liver cirrhosis examined at 7 T showed significantly lower $P_i$ and phosphatidylcholine concentrations and significantly higher glycerophosphoethanolamine concentrations.[171]

The application of high-field $^1$H MRI and $^{31}$P MRSI in human breast at 7 T enables the investigation of phospholipid metabolism, phosphate energy metabolism, and intracellular pH in addition to standard $^1$H applications.[172] At 7 T, altered levels of $^{31}$P metabolites in breast tissue were observed in tumor patients compared with healthy volunteers, and levels were modulated during neoadjuvant chemotherapy.[172] Preliminary results from $^{31}$P MRS at 7 T and subsequent biopsy show that higher numbers of mitosis (proliferation marker) correspond to higher relative concentrations of PME (PME/PDE) in the $^{31}$P spectrum.[128]

In the human prostate, combined $^1$H and $^{31}$P MRSI is feasible at 7 T, which allows, for example, a detailed study of the choline (Cho) metabolism, with negligible efficiency losses in $^1$H MR because of the combined acquisition of $^1$H and $^{31}$P.[153] Furthermore, a recent study demonstrated the feasibility of $^{31}$P MRS in lung carcinoma at 7 T, which may have the potential to be used in addition to standard methods for noninvasive monitoring of treatment response in lung tumors.[173] In dynamic $^{31}$P MRS of the lower leg at 7 T, differences in PCr resynthesis rates could be detected between healthy volunteers and a diabetic patient.[174]

In conclusion, $^{31}$P MR applications at UHF represent a very promising method that may provide new physiological insights in the future.

## Sodium-23 Magnetic Resonance Imaging

Sodium-23 is a spin-3/2 nucleus that exhibits the second highest MR signal in the human body among the MR-detectable nuclei. Especially with increasing availability of UHF MR scanners, the potential of $^{23}$Na MRI has increased because of the linear SNR increase with $B_0$, which is expected for resonance frequencies at least up to approximately 64 MHz (see section Physical Challenges and Advantages of Ultrahigh Field).

Sodium plays a crucial role in many physiologic processes such as the maintenance of cell homeostasis, transmission of action potentials, and regulation of pH, blood volume, and blood pressure. In healthy excitable cells, the concentration of sodium ions in the intracellular space is 5 to 15 mmol/L and in the extracellular space 140 to 150 mmol/L.[137,175] This concentration gradient is maintained, among others, by the

sodium-potassium pump ($Na^+$-$K^+$-ATPase). Therefore, impairment of energy metabolism or disruption of cell membrane integrity will affect the concentration gradient. Determination of sodium concentrations by $^{23}$Na MRI can thus provide information about the tissue state.[175]

Consequently, $^{23}$Na MRI offers a variety of applications for investigating physiologic and pathophysiologic processes in the human body. Comparable to $^{31}$P MR applications, many studies have been performed so far in the head and calf muscle. Here, Staroswiecki et al[176] demonstrated a 2.3-fold higher SNR in the cartilage at 7 T compared with 3 T, which is in accordance with the expected linear increase in SNR with $B_0$. With the development of $^{23}$Na volume coils[177–179] or dedicated $^{23}$Na coils for specific body regions,[180] valuable insights into the torso could also be achieved with $^{23}$Na MRI.[181–184]

### Neuroradiology

A large number of studies have shown that $^{23}$Na MRI is well suited for the investigation of neurodegeneration and neuroinflammation, tumors, energetic imbalances, and excitability disorders.[185]

$^{23}$Na MRI in MS at a field strength of 3 T demonstrated increased tissue sodium concentration (TSC) in acute and chronic lesions but also in normal-appearing white matter compared with healthy controls.[186] A recent study at 7 T further showed a widespread distribution of increased TSC in various MS gray and white matter regions,[187] which complements results obtained at 3 T.[188]

In further studies, a correlation among brain sodium accumulation and disability,[188,189] disease progression,[189] cognitive impairment,[190] and lesion evolution[191] was detected. Furthermore, sodium was found to be a promising tool to monitor patients with progressive MS.[192] A recent study showed that intralesional heterogeneity could be observed when using high-resolution $^{23}$Na MRI if the lesion is of sufficient size.[193,194] More advanced techniques applying triple quantum filtered $^{23}$Na MRI[195] provide information about the intracellular sodium concentration and the intracellular volume fraction in MS.[187] The feasibility of triple quantum filtered $^{23}$Na MRI at 7 T was also demonstrated in patients with MS.[187]

A multitude of further cerebral diseases has been explored with $^{23}$Na MRI, including Huntington disease (HD),[196] AD,[197] cerebral infarction,[198] migraine,[199] and epilepsy.[200]

Furthermore, $^{23}$Na MRI has been applied to cerebral tumors, where, for example, brain tumor growth could be monitored.[201] The TSC is increased in brain tumor tissue.[202] Hence, $^{23}$Na MRI has been investigated for characterizing tumor proliferation[203] and therapy response.[204] Recently, the correlation between TSC and isocitrate dehydrogenase (IDH) mutation status was demonstrated at 7 T.[205] Thus, the spatially resolved information from $^{23}$Na MRI could assist in determining biopsy sites as well as in surgery and radiation therapy.[205]

With the availability of 7 T MR systems as a medical device enabling $^{23}$Na head imaging at 7 T by at least 1 vendor,[138] $^{23}$Na MRI with its increased SNR at UHF offers great potential for future studies in larger patient cohorts.

### Body Applications

Beyond these neurological applications, a variety of body regions and disease conditions have been investigated in initial feasibility studies using $^{23}$Na MR.

$^{23}$Na MRI offers the special possibility of gaining additional insight into the condition of the cartilage, for example, in the knee, because it is sensitive to the glycosaminoglycan (GAG) content.[206] Thus, $^{23}$Na MRI at 7 T can provide insights into cartilage health, repair tissue, and treatment response, for example, in osteoarthritis without the need for a contrast agent.[206] For example, after matrix-associated autologous chondrocyte transplantation, $^{23}$Na MRI enabled a differentiation of repaired tissue from native cartilage, and a correlation was found between $^{23}$Na MRI and dGEMRIC.

Furthermore, $^{23}$Na MRI was investigated in various diseases in which a change in the distribution of muscular $^{23}$Na concentrations is to be expected, for example, in Duchenne muscular dystrophy,[207,208] in dialysis patients,[209] and in diabetic patients.[210,211]

A 7 T $^{23}$Na MRI study in patients with periodic paralysis demonstrated higher muscular $^{23}$Na concentration than in healthy volunteers.[212] Consequently, sodium homeostasis can be visualized in periodic paralysis at 7 T and might be used to evaluate new therapies.

In addition, in both chronic myocardial infarction and after acute myocardial infarction, increased $^{23}$Na signal has been shown in infarcted nonviable myocardium,[181,213,214] and recent methodological work showed that corrections are necessary in $^{23}$Na cardiac MRI to quantitatively estimate concentration values in the myocardium at 7 T.[184]

Furthermore, renal $^{23}$Na MRI has been performed under various physiological conditions, for example, after radiation therapy and after renal transplantation.[183,215,216] Because sodium plays a very important role in renal physiology, $^{23}$Na MRI provides the opportunity to investigate whether kidney function is normal or if any pathological alterations exist.[217,218] Preliminary results of renal $^{23}$Na MRI at 7 T[219] showed the feasibility of an increased spatial resolution with a nominal in-plane resolution of $4 \times 4$ mm$^2$ and a slice thickness of 5 mm compared with studies at 3 T with nominal spatial resolutions of $3 \times 3 \times 15$ mm$^3$[218,220] and $5 \times 5 \times 5$ mm$^3$.[215]

Recent studies on quantitative $^{23}$Na breast MRI at 7 T showed good differentiation between malignant and benign breast lesions and the potential to predict early treatment outcomes of neoadjuvant chemotherapy, with reduced TSC indicating therapy response.[221,222] Further $^{23}$Na studies have investigated lung cancer[223] and prostate tumors.[224]

Hence, $^{23}$Na MRI offers diverse research opportunities, and the reasonable spatial resolutions within clinically feasible measurement times at UHF offer the possibility of bringing these applications into clinical use.

## Further Exotic X-Nuclei

### Potassium-39 and Chlorine-35 Magnetic Resonance Imaging

As with $^{23}$Na MRI (see section Sodium-23 Magnetic Resonance Imaging), MRI of potassium-39 ($^{39}$K) and chlorine-35 ($^{35}$Cl) provides insight into ion balance in humans. These 2 nuclei, in common with $^{23}$Na, have a nuclear spin of 3/2 and undergo quadrupole interaction, which leads to even shorter relaxation times at 7 T compared with $^{23}$Na,[225–227] and because of the even lower MR sensitivity (see Table 1), UHF MRI was needed to pioneer the MRI of $^{39}$K and $^{35}$Cl, with first human applications in the brain and muscle of healthy volunteers.[225,227–229]

Applying $^{35}$Cl MRI at 7 T, pathophysiological changes of $Cl^-$ homeostasis were demonstrated in patients with a tumor and in muscular ion channel disease.[225] Wenz et al[230] recently demonstrated for the first time the feasibility of $^{39}$K MRI of the human heart. This is a very interesting research application, because potassium ions play a crucial role in cardiac electrophysiology, and pathophysiological processes are expected to lead to changes in myocardial $^{39}$K concentration. These initial feasibility studies demonstrate the great potential of X-nuclei MRI at UHF to noninvasively gain insight into ion balance inside the living organism.

### Tracer Nuclei: Oxygen-17, Deuterium, Carbon-13, and Fluorine-19

Several X-nuclei can be used as tracers to monitor metabolic pathways because of their low natural abundance and/or low in vivo concentrations.

Oxygen-17 is a nontoxic and stable oxygen isotope with a nuclear spin of 5/2. Thus, it can be detected by means of $^{17}$O MRI. Because the natural abundance of $^{17}$O is just 0.038%, this isotope can be used as a tracer. When $^{17}$O MR data are obtained while inhaling enriched $^{17}O_2$ gas, these dynamic data enable insights into cerebral oxygen

turnover. By fitting a metabolic model[136] to the dynamic $H_2^{17}O$ signal, the cerebral metabolic rate of oxygen consumption ($CMRO_2$) can be determined in different tissues such as the gray matter, white matter, and tumor tissue.[231] Hence, $^{17}O$ MRI is a promising research technique for the direct investigation of cerebral oxygen metabolism. However, dedicated hardware and acquisition techniques are essential, and the gas is quite expensive. Hence, only a limited number of studies have been performed with $^{17}O$ MRI in humans up to now, all limited to $^{17}O$ brain MRI.

Hoffmann et al[232] obtained the first dynamic $^{17}O$ MR data in a patient with glioblastoma, showing a decreased $CMRO_2$ value within the tumor tissue. Recently, a $^{17}O$ inhalation study including 10 patients with brain tumors was published[233] in which both high-grade and low-grade gliomas exhibited a lower $^{17}O$ MR signal increase in the tumor region and a decrease in tumor $CMRO_2$, which is in accordance with the Warburg effect.

Deuterium ($^2H$) has a nuclear spin of I = 1 and a very low natural abundance. Consequently, deuterium metabolic imaging (DMI) enables the investigation of metabolism in vivo through $^2H$ MRS/MRSI before and after uptake of $^2H$-labeled substrates.[234,235] This novel noninvasive approach was demonstrated in animals[236–239] as well as in healthy volunteers and patients with glioblastoma at $B_0 = 4$ T[234] and has attracted increasing interest from several research groups.[240,241] Recently, it was shown that the sensitivity of DMI increases supralinearly with $B_0$ for small animal coils between 4 and 11.7 T and for larger human coils between 4 and 7 T.[242] According to de Graaf et al,[242] the improved sensitivity at 7 T enables the acquisition of 3D DMI data at a nominal 1 mL spatial resolution. Consequently, DMI is a promising application especially at UHF, where it benefits from the increased SNR and spectral resolution.[242]

Carbon-13 ($^{13}C$) is a constituent of almost all biochemically relevant molecules, and because of its low natural abundance, it can be administered to trace metabolic pathways.[243,244] Heteronuclear coupling can be addressed with $^1H$ decoupling, which collapses multiplets into a singlet resonance and results in an increased SNR and simplification of the spectrum. In general, heteronuclear decoupling is challenging, because it requires transmitting at the $^1H$ frequency while receiving the very low NMR signal at the $^{13}C$ frequency, requiring highly adapted and optimized hardware. Ultrahigh field complicates heterogeneous broadband decoupling because of the high-power deposition (SAR) and the inhomogeneities in the $^1H$ transmit field.[245] Nevertheless, the feasibility of heteronuclear $^1H$ decoupling of $^{13}C$ spectra has been demonstrated in humans in vivo at 7 T.[245] In a $^{13}C$ MRS study at 7 T, patients with glycogen storage disease showed a 2.5-fold increase in muscle glycogen concentrations[246]; these results were also consistent with muscle needle biopsy results. Thus, noninvasive $^{13}C$ MRS could support diagnosis of glycogen storage disease or therapy monitoring.

The NMR properties of $^{19}F$ are comparable to those of protons, leading to a relative sensitivity of 83% compared with $^1H$. However, the abundance of $^{19}F$ in the human body is very low. Thus, fluorinated exogenous compounds can be administered and detected as a tracer, offering high specificity. Up to now, $^{19}F$ MR applications have been limited to in vitro or animal experiments.[247] Studies have investigated, among others, the macrophage response in inflammatory processes[248] or after cerebral infarction.[249] Because fluorine has a similarly high resonance frequency as $^1H$ (see Table 1), hardware and acquisition techniques for $^{19}F$ MRI in humans at 7 T need to be adapted to overcome challenges such as inhomogeneities in the transmit field (see section Radiofrequency Characteristics of $^1H$ at Ultrahigh Field: Issues With Field Inhomogeneity).

## PROTON MAGNETIC RESONANCE SPECTROSCOPY

Proton MRS is used for the direct measurement of metabolites, neurotransmitters, and tissue compositions, all noninvasively. In general, $^1H$ MRS and MRSI at UHF benefit from the increased SNR, larger frequency dispersion, and reduced J-coupling in strongly coupled spin systems.[139] Consequently, various metabolites can be detected, distinguished, and quantified more precisely.[27] However, inhomogeneities in $B_0$, $B_1^+$, $B_1^-$, and SAR at UHF present challenges (see section Physical Challenges and Advantages of Ultrahigh Field) and necessitate new hardware and acquisition techniques.[26,139,250–255] To further improve spectrum quality, both retrospective and prospective motion correction have been suggested.[256]

A detailed overview on advantages, challenges, and advances of UHF $^1H$ MRS/MRSI is given by Henning[139] and by Ladd et al[17] (section 7). In the following subsections, advances in $^1H$ MRS/MRSI applications at UHF in the brain and body are discussed.

### Neuroradiology

Feasibility of single voxel $^1H$ MRS at 7 T to resolve spectral patterns of more than 15 brain metabolites, for example, *myo*-inositol and taurine and overlapping multiplets of J-coupled spin systems, such as glutamine and glutamate (Glu), has been demonstrated by Tkác and colleagues[26] in healthy subjects. Using single voxel $^1H$ MRS at 7 T, studies have reported sufficient sensitivity to detect changes caused by functional activity (eg, visual stimulation) for concentration changes greater than 0.2 μmol/g at 7 T.

In patients with glioma, 7 T MRI extends the available metabolite maps compared with 3 T approaches, which allows the assessment of an extended neurochemical profile in shorter acquisition time.[257] Because of the critical relevance of the IDH mutation status for diagnosis and prognosis of patients with glioma, strong efforts have been made to develop MRI approaches to identify the IDH mutation status noninvasively.[258] Magnetic resonance spectroscopy of 2-hydroxyglutarate (2-HG) has gained considerable attention, because the oncometabolite 2-HG is known to accumulate in gliomas with mutations in the *IDH1*/*2* genes. At 3 T, detection of 2-HG has been demonstrated to be feasible but remains challenging in clinical practice.[259] Therefore, 2-HG MRS at 7 T with increased SNR and spectral resolution could be capable of differentiating IDH mutation from wildtype brain tumors more reliably without the need for invasive procedures.[260]

In patients with MS, MRS biomarkers such as glutathione, γ-aminobutyric acid, Glu, and others demonstrated the potential of UHF MRI to aid lesion characterization that could help in clinical decision making.[261]

Seven Tesla MRS has also been applied in patients with amyotrophic lateral sclerosis, showing decreased *N*-acetylaspartate (NAA) and Glu in subjects with amyotrophic lateral sclerosis compared with healthy controls.[262] The study findings indicate neuronal injury and/or loss in the precentral gyrus associated with the disease.

Investigations of 7 T MRS in patients with HD revealed decreased concentrations of NAA and creatine in the caudate nucleus and putamen of early manifest HD, suggesting deficits in neuronal integrity and energy metabolism.[263]

In patients with AD, 7 T MRS revealed several region-specific effects of MCI on brain metabolite levels.[264] In a pilot study, Oeltzschner et al[264] found MCI to be associated with decreased γ-aminobutyric acid and Glu levels, most consistently in the posterior cingulate cortex.

Magnetic resonance spectroscopic imaging at UHF offers the possibility to assess region-specific heterogeneity of metabolic profiles in various diseases. The introduction of ultrashort echo time sequences, such as, for example, free induction decay (FID) MRSI, aids avoiding SNR loss because of short $T_2$ relaxation.[265,266] Free induction decay MRSI has therefore improved detectability of low concentration metabolites at higher spatial resolutions.[265,266] Comparison of spectral quality of high-resolution FID MRSI at 3 T and 7 T demonstrates clear improvement in spectra quality and quantification precision for 7 T FID MRSI (Fig. 7).[267]

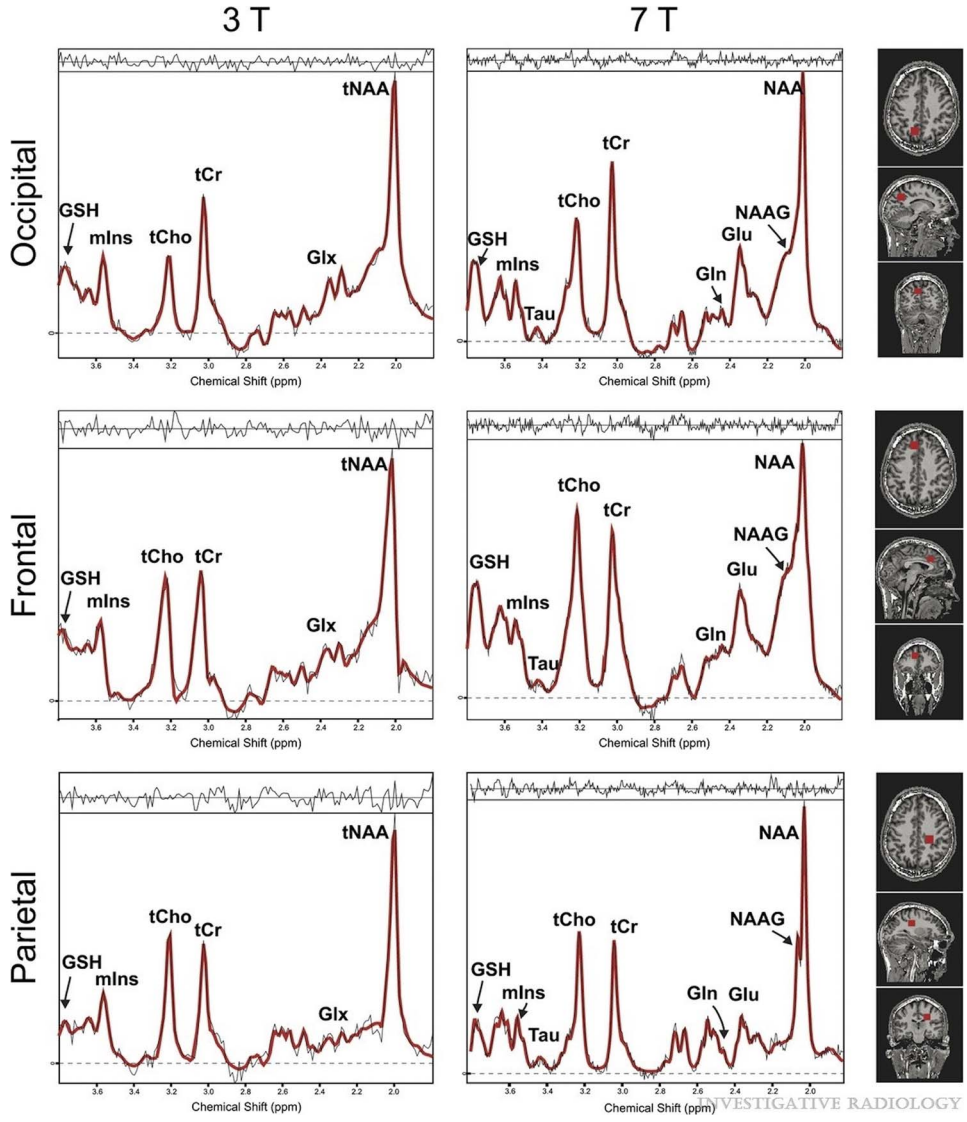


**FIGURE 7.** Sample spectra overlaid with the LCModel fit (red color) at 3 T (left column) and 7 T (right column) from 3 different locations: occipital lobe (top), frontal lobe (middle), and parietal lobe (bottom). For instance, note the tNAA signal at 7 T. The better spectral resolution allows differentiation of NAA and NAAG at 7 T, but not at 3 T (measurement parameters: excitation flip angle, 45 degrees; field of view, 220 × 220 $mm^2$; 64 × 64 matrix; TR, 600 milliseconds; TE*, 1.5 milliseconds; bandwidth, 6000 Hz; 2048 points; and 10-mm slice thickness). Reused with permission from Wolters Kluwer Health, Inc, Gruber et al.[267]

At 9.4 T, high-resolution metabolite maps (97 μL nominal voxel size, 18 brain metabolites) have been acquired by Nassirpour et al[268] by combining an improved sensitivity encoding (SENSE) reconstruction with a $B_0$ correction of spatially overdiscretized MRSI data. With SENSE and GRAPPA, entire k-space lines are omitted. To achieve higher accelerations compared with 2D parallel imaging methods in multislice MRSI, the 2D CAIPIRINHA approach has been suggested, where k-space points are skipped in arbitrary patterns.[269] Furthermore, spatial-spectral encoding (eg, rings, spirals) yields high acceleration factors of up to 2 orders of magnitude.[270]

Hingerl and colleagues[271] applied FID MRSI with a rapid concentric ring trajectory at 7 T for metabolic mapping of the whole cerebrum (8 metabolites) in healthy subjects, 1 patient with glioma and another patient with MS. In tumor tissue, Cho, glutamine, and glycine were markedly increased compared with normal-appearing brain regions.[271]

Hangel et al[272] combined MRSI with patch-based superresolution reconstruction for high-resolution multimetabolite mapping of gliomas and demonstrated metabolic activities beyond morphologically visible deviations.

The previously discussed role of the oncometabolite 2-HG in IDH-mutant gliomas has also motivated the development of 3D MRSI targeting 2-HG, for example, using MEGA (Mescher-Garwood) and LASER (localization by adiabatic selective refocusing).[273,274] Andronesi et al[274] showed that 3D dynamic measurements of 2HG are feasible, and that changes in IDH associated with therapy response can be monitored in patients with IDH-mutant gliomas. The monitoring of treatment response and patient follow-up is of particular interest for the application of imaging biomarkers in cancer, because serial biopsies are usually not feasible.

## Body Applications

Seven Tesla MRS has the potential to become an important tool in clinical MSK MRI because of its noninvasive sensitivity to metabolic tissue features.

Investigations of lipid metabolism of the human calf muscle at 7 T showed accurate and reliable spectroscopic examination by both 1D and 2D MRS.[275] Estimates of intramyocellular lipids and extramyocellular lipids could be improved by including variations in fiber orientation in the lineshape analysis.[276] The 2D approach has offered improved resolution and sensitivity compared with previous reports at lower field strength and improved opportunities to study disease effects in muscles.[275]

The feasibility of prostate $^{1}$H MRSI at 7 T has been demonstrated by Lagemaat et al,[277] who used a low-power spectral-spatial pulse sequence while using separate transmit and receive coils. The low-SAR MRSI concept provided the opportunity to increase spatial resolution of MRSI within reasonable scan times.[277]

Breast $^{1}$H MRS at 7 T has been investigated in a pilot study by Korteweg et al[278] using a 2-channel coil setup. The obtained spectra in patients with breast cancer showed a decrease in Cho concentrations during neoadjuvant chemotherapy, suggesting responsiveness to treatment.[278]

## FUNCTIONAL MAGNETIC RESONANCE IMAGING FOR MAPPING NEURONAL ACTIVITY

Mapping neuronal activity in the human brain can be performed via so-called fMRI. As standard, the BOLD (blood-oxygen-level-dependent) effect is used for this purpose, which exploits the fact that oxyhemoglobin (oxygenated hemoglobin) is diamagnetic, whereas deoxyhemoglobin (deoxygenated hemoglobin) is paramagnetic.[279–281] Neuronal activity leads to increased oxygen consumption, which is overcompensated by an increased cerebral blood flow. As a result, more oxyhemoglobin is present during activation, which causes fewer susceptibility-induced field perturbations in the local magnetic field, leading to reduced spin dephasing and a lower relaxation rate $R_2$*. Consequently, the signal in activated brain regions is higher in $T_2$*- and $T_2$-weighted MR images. As mentioned in the section Physical Challenges and Advantages of Ultrahigh Field, higher magnetic fields provide increased susceptibility sensitivity and thus also an enhanced BOLD effect.[282,283]

Because of the expectation of a supralinear increase in BOLD sensitivity[284] as well as improved spatial localization[285] with static magnetic field strength, fMRI represents one of the driving forces in the development of UHF systems.[286,287] However, poorer static magnetic field homogeneity and poorer $B_1^+$ homogeneity complicate fMRI at UHF. Here, the use of pTx can lead to a significant improvement. A detailed overview on the underlying biophysics of the BOLD contrast as well as on pulse sequences and applications at UHF is given by Marques and Norris[288] and by Ladd et al[17] (section 9).

### Neuroradiology

The spatial resolution at 3 T is limited to approximately 2 mm$^3$, whereas at 7 T, a resolution of approximately 1 mm$^3$ can be achieved.[289] Submillimeter resolutions were also obtained at 7 T, for example, 0.65 mm$^3$ for visual stimulation and 0.75 mm$^3$ for sensorimotor stimulation.[290] Thus, UHF fMRI enables improved mapping of neuronal activity in the cortex,[291,292] cerebellum,[293,294] and subcortical structures.[295,296] Recently, a submillimeter resolution of 0.75 mm$^3$ was achieved in resting state fMRI while applying the method to a macaque at a field strength of 10.5 T.[287]

Comparing 3 T to 7 T fMRI, a study in 17 patients showed that a simple motor task resulted in increased activation in the primary motor cortex at 7 T. However, ghosting and motion artifacts were more prevalent at 7 T.[297]

In addition to the main applications of UHF fMRI to study neuronal activity at high spatial resolution, further promising areas of research are focused on fMRI of the cortical layers and columns.[298–302] Thus far, however, UHF fMRI has been less extensively evaluated for clinical application, for example, for presurgical planning.[303,304]

## CHEMICAL EXCHANGE-SENSITIVE MAGNETIC RESONANCE IMAGING

Chemical exchange-sensitive MRI techniques are based on the chemical exchange between solute-bound protons and protons of free bulk water. One type of chemical exchange-sensitive MRI that has recently gained considerable attention is CEST MRI.[305] Chemical exchange saturation transfer MRI permits large signal amplification of low-concentration molecules in vivo. The amide proton transfer (APT) effect is most commonly assessed with CEST MRI. Amide proton transfer effects resonate at approximately +3.5 parts per million relative to the water proton resonance. Amide proton transfer signal quantification is usually achieved using the MT ratio asymmetry approach proposed by Zhou et al.[306] By providing information on protein concentration and microenvironmental tissue features, CEST MRI

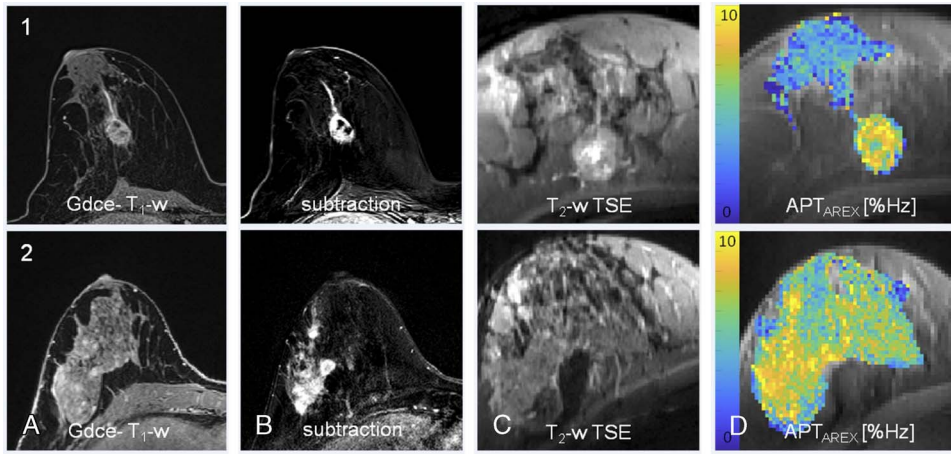


**FIGURE 8.** Relaxation-compensated APT CEST-MRI at 7 T and clinical MR mammography. Patient 1: high grade/patient 2: intermediate grade intraductal breast cancer of no special type. In both patients, a strong gadolinium enhancement can be observed at clinical MRI: gadolinium-enhanced (Gdce), fat-saturated $T_1$-weighted MRI after administration of a standard dose (0.1 mmol/kg body weight) of gadobutrol (TR, 28 milliseconds; TE, 4.76 milliseconds; slice thickness, 1.1 mm; flip angle, 25; field of view, 360; matrix, 320) and subtraction MRI. In addition, $T_2$-weighted TSE (1c, 2c) and the $APT_{AREX}$ contrasts at 7 T are shown. All breast cancers could be clearly identified on the $APT_{AREX}$ contrast. APT signal hyperintensities showed a distinct morphological correlation with the contrast-enhanced MR images. Reproduced with permission from Elsevier, Loi et al.[335]

extends the available repertoire of MR biomarkers in diagnostic radiology.[307] Ultrahigh field scanners have enabled the acquisition of highly resolved spectral data that permit more sophisticated signal quantifications, which include the correction of confounding effects such as direct water saturation (spillover), conventional broad MT, and interference with other metabolite resonances, for example, by using multipool Lorentzian fit analysis.[307–312] These approaches also allow quantification of multiple CEST pools simultaneously, for example, relayed nuclear Overhauser effects (rNOEs) and amine resonances.[305] Generally, GRE-based acquisition provides a robust readout method for CEST at UHF. For spiral-centric reordered k-space acquisition, Zaiss et al[313] demonstrated with their Snapshot-CEST approach that the image quality can be further improved using a rectangular spiral reordering scheme adjusted to the field of view.

## Neuroradiology

Studies of APT MRI assessing therapy response in patients with glioma found increased APT signals in tumors lesions with progressive disease compared with treatment-related changes or residual tumors classified as stable disease.[307,314–317] In patients with newly diagnosed glioma, APT and rNOE CEST signals are associated with response to first-line therapy as reported in several studies.[307,316,318,319] Amide proton transfer mediated CEST effects have been shown to be associated with World Health Organization tumor grade and cellularity[320–325] and to be correlated with the IDH mutation status in gliomas.[324,326] Highest sensitivity and specificity for IDH status prediction were achieved at 7 T using the downfield rNOE-suppressed APT metric.[324] Relayed nuclear Overhauser effect imaging at 7 T has also been found to be associated with tumor grade[327,328] and cellularity.[329] For 7 T APT imaging at initial diagnosis of patients with glioma, an inverse signal correlation with overall survival and progression-free survival has been found.[307,319]

The majority of CEST studies at UHF have been applied in neuro-oncological diseases. At 3 T MRI, a broader spectrum of neurological diseases has already been investigated. Recently, a multipool CEST MRI approach has been demonstrated to be feasible at 7 T in patients with acute ischemic stroke.[330] In addition, APT imaging at 7 T has been applied to study radionecrosis after stereotactic radiosurgery of AVM.[331]

For the detection of Glu in the human brain, GluCEST MRI has been proposed by Davis et al.[332] GluCEST signals have been shown to enable correct lateralization in temporal lobe seizure.[332] Moreover, peritumoral GluCEST signals were associated with recent seizures and drug-refractory epilepsy in patients with glioma.[333]

## Body Applications

Chemical exchange saturation transfer MRI has also been applied in other organs and diseases at UHF, whereas a much wider range of applications has been explored at 3 T field strength. Investigations in patients with breast cancer at 7 T showed a positive correlation between APT CEST signal intensity and tumor cellularity[334–336] and indicated that APT CEST may enable detection of early therapy response during neoadjuvant chemotherapy.[337] Figure 8 shows 2 patients with biopsy-proven breast cancer. Increased APT signals at 7 T corresponded well with gadolinium contrast-enhancement in the tumor region.

For MSK applications, the detection of GAGs of articular cartilage at 7 T has been demonstrated.[338,339] A major advantage of gagCEST compared with other GAG-sensitive MRI techniques, such as sodium MRI and dGEMRIC, is the comparably short acquisition time for full 3D coverage of a knee joint in approximately 10 minutes.[339]

## Exogenous Chemical Exchange Saturation Transfer Agents

The CEST contrast produced by a probe depends on multiple parameters including concentration, proton exchange rate, number of exchangeable protons, $T_1$, $T_2$, saturation scheme, and so on.[340] The use of exogenous agents to generate contrast via chemical exchange generally faces the challenge of relatively low in vivo sensitivity. However, sensitivity can be improved by using agents that accumulate in the diseased tissue.[341]

One biodegradable agent that has recently gained considerable attention is natural D-glucose for dynamic glucose-enhanced (DGE) MRI. The indirect detection of glucose via chemical exchange-sensitive MRI (ie, CEST or chemical exchange-sensitive spin-lock [CESL]) enables strong signal amplification. The detected signal is proportional to the local concentration change of glucose after intravenous administration.[342] Demonstrations of feasibility of DGE MRI in patients with glioma were performed by Xu et al[343] using CEST and by Schuenke et al[344,345] and Paech et al[346] using adiabatically prepared CESL MRI. Glucose contrast enhancement has been reported, especially in areas of disrupted blood-brain barrier (BBB), suggesting major signal contributions from BBB leakage and tissue perfusion.[343–347]

However, increased glucose concentrations were also found in areas outside the disrupted BBB.[344,346] In contrast to gadolinium-based contrast agents, glucose is not confined to the intravascular space and the extracellular extravascular space. Furthermore, CEST and CESL signals may also be altered by local pH, because an acidic microenvironment may modulate the proton exchange rate.[348]

It must be noted that DGE MRI contrasts are prone to motion-induced artifacts and therefore require sophisticated motion correction approaches.[349,350] At 3 T field strength, small effect sizes currently limit robust signal quantification.[351,352] Dynamic glucose-enhanced MRI may therefore profit from the fact that the number of UHF scanners in clinical units is continuously increasing, possibly paving the way for wider clinical exploration.

# BEYOND 7 T

In the future, further increases in field strength will advance our capabilities in clinical research and assuredly lead to significant advances in these MRI techniques, although they will initially not be applied for the clinical workup of individual patients. As mentioned in the introduction, there is already 1 human MRI system operating at 10.5 T and 3 systems operating at 11.7 T are in the process of installation. Scientifically, the rationale for going to even higher magnetic fields are clear,[353–355] and plans to implement MRI systems at 14 T are being pursued in several countries around the world, including China, Germany, the Netherlands, and the United States. In particular, the magnets of these systems represent a significant engineering challenge, because niobium-titanium, the superconductor almost exclusively used for human MRI magnets up to 11.7 T, is no longer a viable alternative at higher magnetic fields. A 14 T magnet will have to incorporate at least some niobium-tin or high-temperature superconducting materials with superior superconducting performance parameters.[356] These materials are more expensive and more difficult to manufacture than niobium-titanium, so financing a 14 T MRI system will be an economic in addition to technical challenge; however, preliminary design studies indicate that, because of the higher material performance, less superconducting wire is needed overall than with a scaled-up niobium-titanium design, so the cost and magnet size do not scale as severely as expected.

Ultimately, the upper limit on magnetic field strength for human MRI will be set by physiologic, not technical considerations. Human studies up to 10.5 T have thus far failed to reveal any severe or permanent physiologic effects related to the magnetic field,[357] that is, no significant cognitive effects or increases in blood pressure or heart rate. Animal studies in rats suspended in a vertical 14 T field showed that there were significant interactions with the vestibular system,[358] leading to the animals circling in a preferred direction after exposure. However, the authors noted that the orientation of the human vestibular system to the main magnetic field in a classical solenoidal design with the magnetic field along the axis of the body is less conducive to inducing the observed effects, so that they postulated that 14 T exposure might not have

similar consequences in humans.[358] Further research on the physiologic underpinnings of vestibular interactions supports this supposition,[359] as the main mechanism is now considered to be related to ionic currents in the endolymph of the inner ear interacting with the main magnetic field. The orientation of ionic flow relative to the magnetic field determines the severity of the effects, and the vector cross product is lower in humans than in rats or mice. Another area of physiologic interaction is magnetohydrodynamic effects that occur in the electrically conducting flowing blood. Experimentally unconfirmed theoretical calculations indicate that volume flow rate in the aorta might be reduced by roughly 10% at 15 T,[360] leading to regulatory compensation in heart rate or blood pressure. Thus, although physiologic considerations are not expected to limit MRI application up to 14 T, these aspects will have to be critically examined with each elevation in field strength.

Systems beyond 7 T are all targeted toward fundamental research, either for studying brain function or for understanding healthy human physiology and aging or the pathophysiology of various diseases. Given the challenges involved, it is unlikely that any field strength beyond 7 T will be considered for diagnosis in individual patients for at least a couple of decades. However, knowledge gained with such systems about disease processes in groups of individuals and associated technological advancements may "trickle down" to lower field strength systems that are used clinically.

## SUMMARY

Although UHF MRI has been the subject of intense research for over 2 decades, several significant challenges remain. Most pressing currently is the need for clinical approval of pTx technology including multichannel transmit RF coils that can expand the application domain outside the brain and small joints to the thorax, abdomen, pelvis, and specific organs such as the breasts. pTx technology will not only facilitate excellent image quality throughout the body, but could also facilitate the examination of patients with implants, who represent a continually increasing proportion of the patient population as implants become more widespread. Only very few implants have thus far been certified as MR-conditional for 7 T.[124] Beyond the obvious danger of magnetic forces and torques, RF interactions and heating around the implants is of concern, and pTx can help by modulating the electric RF field responsible for heating.[361,362] Finally, even if all the technical challenges can be satisfactorily resolved, the role of 7 T in the clinical workup of patients will be strongly influenced by economic considerations. A 7 T examination is definitely more expensive than an examination at 3 T or 1.5 T, but to secure higher reimbursement rates, 7 T must demonstrate enhanced clinical value, and this is still an ongoing process.

Despite these outstanding challenges, the introduction of UHF scanners has already had a major influence on the possibilities in clinical neuro and MSK MRI. Advanced clinical evidence of added diagnostic value has for instance been demonstrated in patients with epilepsy by the "7 T Epilepsy Task Force" through the collection of over 2000 data sets from twenty-one 7 T MRI centers.[92] All MRI techniques, including SWI, MPRAGE, as well as TOF MRA, profit considerably from the boost in SNR and CNR, which permits high-resolution MRI. This enables the precise visualization of anatomical substructures or cerebral blood flow or cartilage disease, greatly benefiting clinical decision making. Furthermore, UHF proton MRI permits the identification of novel MR biomarkers that provide information about diseases such as brain cancer or epilepsy. In addition to this gain in morphological information, UHF MRI enhances the specificity of fMRI techniques. In fMRI, advances in field strength permit submillimeter detection of the BOLD signal, providing insights into brain connectivity. The advent of UHF scanners has sparked significant progress in preclinical techniques such as CEST MRI, DGE MRI, or X-nuclei MRI, techniques that furnish metabolic information about physiological and pathophysiological processes. In the near future, all these promising methods and encouraging results need to translate into clinical evidence, which requires dedicated, large-cohort prospective trials to prove patient benefit. Ultrahigh field MRI already plays a key role in neuroscience and preclinical research into disease pathology, and its role in clinical diagnostics is sure to expand as more systems with clinical approval as medical devices are installed and its added value in the clinic is established and validated.

## REFERENCES


1. Robitaille PM, Warner R, Jagadeesh J, et al. Design and assembly of an 8 Tesla whole-body MR scanner. *J Comput Assist Tomogr*. 1999;23:808–820.
2. Bourekas EC, Christoforidis GA, Abduljalil AM, et al. High resolution MRI of the deep gray nuclei at 8 Tesla. *J Comput Assist Tomogr*. 1999;23:867–874.
3. Burgess RE, Yu Y, Christoforidis GA, et al. Human leptomeningeal and cortical vascular anatomy of the cerebral cortex at 8 Tesla. *J Comput Assist Tomogr*. 1999;23:850–856.
4. Vaughan JT, Garwood M, Collins CM, et al. 7T vs. 4T: RF power, homogeneity, and signal-to-noise comparison in head images. *Magn Reson Med*. 2001;46: 24–30.
5. Yacoub E, Shmuel A, Pfeuffer J, et al. Imaging brain function in humans at 7 Tesla. *Magn Reson Med*. 2001;45:588–594.
6. Novak P, Novak V, Kangarlu A, et al. High resolution MRI of the brainstem at 8 T. *J Comput Assist Tomogr*. 2001;25:242–246.
7. Norris DG. High field human imaging. *J Magn Reson Imaging*. 2003;18:519–529 Available at: https://doi.org/10.1186/1532-429X-15-S1-W21. Accessed August 23, 2021.
8. United States Food and Drug Administration. 2017. Available at: https://www.fda.gov/news-events/press-announcements/fda-clears-first-7t-magnetic-resonance-imaging-device. Accessed April 2021.
9. Erturk MA, Wu X, Eryaman Y, et al. Toward imaging the body at 10.5 Tesla. *Magn Reson Med*. 2017;77:434–443.
10. Le Bihan D, Schild T. Human brain MRI at 500 MHz, scientific perspectives and technological challenges. *Supercond Sci Technol*. 2017;30:033003.
11. Edelstein WA, Glover GH, Hardy CJ, et al. The intrinsic signal-to-noise ratio in NMR imaging. *Magn Reson Med*. 1986;3:604–618.
12. Pohmann R, Speck O, Scheffler K. Signal-to-noise ratio and MR tissue parameters in human brain imaging at 3, 7, and 9.4 Tesla using current receive coil arrays. *Magn Reson Med*. 2016;75:801–809.
13. Guerin B, Villena JF, Polimeridis AG, et al. The ultimate signal-to-noise ratio in realistic body models. *Magn Reson Med*. 2017;78:1969–1980.
14. von Morze C, Xu D, Purcell DD, et al. Intracranial time-of-flight MR angiography at 7T with comparison to 3T. *J Magn Reson Imaging*. 2007;26:900–904.
15. Schewzow K, Fiedler GB, Meyerspeer M, et al. Dynamic ASL and T2-weighted MRI in exercising calf muscle at 7 T: a feasibility study. *Magn Reson Med*. 2015; 73:1190–1195.
16. Moser E, Stahlberg F, Ladd ME, et al. 7-T MR—from research to clinical applications? *NMR Biomed*. 2012;25:695–716.
17. Ladd ME, Bachert P, Meyerspeer M, et al. Pros and cons of ultra-high-field MRI/MRS for human application. *Prog Nucl Magn Reson Spectrosc*. 2018;109:1–50.
18. Duyn JH, van Gelderen P, Li TQ, et al. High-field MRI of brain cortical substructure based on signal phase. *Proc Natl Acad Sci U S A*. 2007;104:11796–11801.
19. Peters AM, Brookes MJ, Hoogenraad FG, et al. T2* measurements in human brain at 1.5, 3 and 7 T. *Magn Reson Imaging*. 2007;25:748–753.
20. Wu W, Miller KL. Image formation in diffusion MRI: a review of recent technical developments. *J Magn Reson Imaging*. 2017;46:646–662.
21. Uğurbil K, Xu J, Auerbach EJ, et al. Pushing spatial and temporal resolution for functional and diffusion MRI in the human connectome project. *Neuroimage*. 2013;80:80–104.
22. Wu W, Poser BA, Douaud G, et al. High-resolution diffusion MRI at 7T using a three-dimensional multi-slab acquisition. *Neuroimage*. 2016;143:1–14.
23. Vu AT, Auerbach E, Lenglet C, et al. High resolution whole brain diffusion imaging at 7T for the human connectome project. *Neuroimage*. 2015;122:318–331.
24. Heidemann RM, Anwander A, Feiweier T, et al. K-space and q-space: combining ultra-high spatial and angular resolution in diffusion imaging using ZOOPPA at 7 T. *Neuroimage*. 2012;60:967–978.
25. Frost R, Jezzard P, Douaud G, et al. Scan time reduction for readout-segmented EPI using simultaneous multislice acceleration: diffusion-weighted imaging at 3 and 7 Tesla. *Magn Reson Med*. 2015;74:136–149.
26. Tkác I, Andersen P, Adriany G, et al. In vivo 1H NMR spectroscopy of the human brain at 7 T. *Magn Reson Med*. 2001;46:451–456.
27. Yang S, Hu J, Kou Z, et al. Spectral simplification for resolved glutamate and glutamine measurement using a standard STEAM sequence with optimized timing parameters at 3, 4, 4.7, 7, and 9.4T. *Magn Reson Med*. 2008;59:236–244.

28. Zaiss M, Bachert P. Chemical exchange saturation transfer (CEST) and MR Z-spectroscopy in vivo: a review of theoretical approaches and methods. *Phys Med Biol*. 2013;58:R221–R269.
29. Fiedler TM, Ladd ME, Bitz AK. SAR simulations & safety. *Neuroimage*. 2018; 168:33–58.
30. Vaidya MV, Collins CM, Sodickson DK, et al. Dependence of B1+ and B1- field patterns of surface coils on the electrical properties of the sample and the MR operating frequency. *Concepts Magn Reson Part B Magn Reson Eng*. 2016;46: 25–40.
31. Orzada S, Maderwald S, Poser BA, et al. RF excitation using time interleaved acquisition of modes (TIAMO) to address B1 inhomogeneity in high-field MRI. *Magn Reson Med*. 2010;64:327–333.
32. Metzger GJ, Auerbach EJ, Akgun C, et al. Dynamically applied B1+ shimming solutions for non-contrast enhanced renal angiography at 7.0 Tesla. *Magn Reson Med*. 2013;69:114–126.
33. Padormo F, Beqiri A, Hajnal JV, et al. Parallel transmission for ultrahigh-field imaging. *NMR Biomed*. 2016;29:1145–1161.
34. Gras V, Vignaud A, Amadon A, et al. Universal pulses: a new concept for calibration-free parallel transmission. *Magn Reson Med*. 2017;77:635–643.
35. Herrler J, Liebig P, Gumbrecht R, et al. Fast online-customized (FOCUS) parallel transmission pulses: a combination of universal pulses and individual optimization. *Magn Reson Med*. 2021;85:3140–3153.
36. Kraff O, Fischer A, Nagel AM, et al. MRI at 7 Tesla and above: demonstrated and potential capabilities. *J Magn Reson Imaging*. 2015;41:13–33.
37. Ren J, Shang T, Sherry AD, et al. Unveiling a hidden $^{31}$ P signal coresonating with extracellular inorganic phosphate by outer-volume-suppression and localized $^{31}$ P MRS in the human brain at 7T. *Magn Reson Med*. 2018;80:1289–1297.
38. Du F, Zhu XH, Qiao H, et al. Efficient in vivo 31P magnetization transfer approach for noninvasively determining multiple kinetic parameters and metabolic fluxes of ATP metabolism in the human brain. *Magn Reson Med*. 2007;57: 103–114.
39. Andre JB, Bresnahan BW, Mossa-Basha M, et al. Toward quantifying the prevalence, severity, and cost associated with patient motion during clinical MR examinations. *J Am Coll Radiol*. 2015;12:689–695.
40. Zaitsev M, Maclaren J, Herbst M. Motion artifacts in MRI: a complex problem with many partial solutions. *J Magn Reson Imaging*. 2015;42:887–901.
41. Federau C, Gallichan D. Motion-correction enabled ultra-high resolution in-vivo 7T-MRI of the brain. *PloS One*. 2016;11:e0154974.
42. Lüsebrink F, Sciarra A, Mattern H, et al. $T_1$-weighted in vivo human whole brain MRI dataset with an ultrahigh isotropic resolution of 250 μm. *Sci Data*. 2017; 4:170032.
43. Mattern H, Sciarra A, Lüsebrink F, et al. Prospective motion correction improves high-resolution quantitative susceptibility mapping at 7T. *Magn Reson Med*. 2019;81:1605–1619.
44. Zwanenburg JJ, Hendrikse J, Visser F, et al. Fluid attenuated inversion recovery (FLAIR) MRI at 7.0 Tesla: comparison with 1.5 and 3.0 Tesla. *Eur Radiol*. 2010; 20:915–922.
45. Theysohn JM, Kraff O, Maderwald S, et al. The human hippocampus at 7 T—in vivo MRI. *Hippocampus*. 2009;19:1–7.
46. Springer E, Dymerska B, Cardoso PL, et al. Comparison of routine brain imaging at 3 T and 7 T. *Invest Radiol*. 2016;51:469–482.
47. Paech D, Kuder TA, Roßmanith C, et al. What remains after transient global amnesia (TGA)? An ultra-high field 7 T magnetic resonance imaging study of the hippocampus. *Eur J Neurol*. 2020;27:406–409.
48. Gizewski ER, Maderwald S, Linn J, et al. High-resolution anatomy of the human brain stem using 7-T MRI: improved detection of inner structures and nerves? *Neuroradiology*. 2014;56:177–186.
49. Straub S, Knowles BR, Flassbeck S, et al. Mapping the human brainstem: brain nuclei and fiber tracts at 3 T and 7 T. *NMR Biomed*. 2019;32:e4118.
50. Duyn JH. Study of brain anatomy with high-field MRI: recent progress. *Magn Reson Imaging*. 2010;28:1210–1215.
51. Abduljalil AM, Schmalbrock P, Novak V, et al. Enhanced gray and white matter contrast of phase susceptibility-weighted images in ultra-high-field magnetic resonance imaging. *J Magn Reson Imaging*. 2003;18:284–290.
52. Dammann P, Barth M, Zhu Y, et al. Susceptibility weighted magnetic resonance imaging of cerebral cavernous malformations: prospects, drawbacks, and first experience at ultra-high field strength (7-Tesla) magnetic resonance imaging. *Neurosurg Focus*. 2010;29:E5.
53. Hosseini Z, Matusinec J, Rudko DA, et al. Morphology-specific discrimination between MS white matter lesions and benign white matter hyperintensities using ultra-high-field MRI. *AJNR Am J Neuroradiol*. 2018;39:1473–1479.
54. Reichenbach JR, Venkatesan R, Schillinger DJ, et al. Small vessels in the human brain: MR venography with deoxyhemoglobin as an intrinsic contrast agent. *Radiology*. 1997;204:272–277.
55. Dieleman N, van der Kolk AG, Zwanenburg JJ, et al. Imaging intracranial vessel wall pathology with magnetic resonance imaging: current prospects and future directions. *Circulation*. 2014;130:192–201.
56. Heverhagen JT, Bourekas E, Sammet S, et al. Time-of-flight magnetic resonance angiography at 7 Tesla. *Invest Radiol*. 2008;43:568–573.
57. Wrede KH, Dammann P, Johst S, et al. Non-enhanced MR imaging of cerebral arteriovenous malformations at 7 Tesla. *Eur Radiol*. 2016;26:829–839.
58. Wrede KH, Matsushige T, Goericke SL, et al. Non-enhanced magnetic resonance imaging of unruptured intracranial aneurysms at 7 Tesla: comparison with digital subtraction angiography. *Eur Radiol*. 2017;27:354–364.
59. Matsushige T, Kraemer M, Schlamann M, et al. Ventricular microaneurysms in Moyamoya angiopathy visualized with 7T MR angiography. *AJNR Am J Neuroradiol*. 2016;37:1669–1672.
60. Schmitter S, Jagadeesan B, Grande A, et al. 4D flow measurements in the superior cerebellar artery at 7 Tesla: feasibility and potential for applications in patients with trigeminal neuralgia. *J Cardiovasc Magn Reson*. 2013;15: W21. Available at: https://doi.org/10.1186/1532-429X-15-S1-W21. Accessed August 23, 2021.
61. Schnell S, Wu C, Ansari SA. 4D MRI flow examinations in cerebral and extracerebral vessels. Ready for clinical routine? *Curr Opin Neurol*. 2016;29: 419–428.
62. De Cocker LJ, Lindenholz A, Zwanenburg JJ, et al. Clinical vascular imaging in the brain at 7T. *Neuroimage*. 2018;168:452–458.
63. Novak V, Abduljalil AM, Novak P, et al. High-resolution ultrahigh-field MRI of stroke. *Magn Reson Imaging*. 2005;23:539–548.
64. Van Veluw SJ, Zwanenburg JJ, Engelen-Lee J, et al. In vivo detection of cerebral cortical microinfarcts with high-resolution 7T MRI. *J Cereb Blood Flow Metab*. 2013;33:322–329.
65. Fracasso A, van Veluw SJ, Visser F, et al. Lines of Baillarger in vivo and ex vivo: myelin contrast across lamina at 7T MRI and histology. *Neuroimage*. 2016;133: 163–175.
66. Van Dalen JW, Scuric EE, Van Veluw SJ, et al. Cortical microinfarcts detected in vivo on 3 Tesla MRI: clinical and radiological correlates. *Stroke*. 2015;46: 255–257.
67. Weller M, van den Bent M, Hopkins K, et al. EANO guideline for the diagnosis and treatment of anaplastic gliomas and glioblastoma. *Lancet Oncol*. 2014;15: e395–e403.
68. Compter I, Peerlings J, Eekers DB, et al. Technical feasibility of integrating 7 T anatomical MRI in image-guided radiotherapy of glioblastoma: a preparatory study. *MAGMA*. 2016;29:591–603.
69. Regnery S, Knowles BR, Paech D, et al. High-resolution FLAIR MRI at 7 Tesla for treatment planning in glioblastoma patients. *Radiother Oncol*. 2019;130: 180–184.
70. Noebauer-Huhmann IM, Szomolanyi P, Kronnerwetter C, et al. Brain tumours at 7T MRI compared to 3T—contrast effect after half and full standard contrast agent dose: initial results. *Eur Radiol*. 2015;25:106–112.
71. Lupo JM, Chuang CF, Chang SM, et al. 7-Tesla susceptibility-weighted imaging to assess the effects of radiotherapy on normal-appearing brain in patients with glioma. *Int J Radiat Oncol Biol Phys*. 2012;82:e493–e500.
72. Radbruch A, Eidel O, Wiestler B, et al. Quantification of tumor vessels in glioblastoma patients using time-of-flight angiography at 7 Tesla: a feasibility study. *PLoS One*. 2014;9:e110727.
73. Filippi M, Evangelou N, Kangarlu A, et al. Ultra-high-field MR imaging in multiple sclerosis. *J Neurol Neurosurg Psychiatry*. 2014;85:60–66.
74. Kollia K, Maderwald S, Putzki N, et al. First clinical study on ultra-high-field MR imaging in patients with multiple sclerosis: comparison of 1.5T and 7T. *AJNR Am J Neuroradiol*. 2009;30:699–702.
75. Waiczies S, Els A, Kuchling J, et al. Magnetic resonance imaging of multiple sclerosis at 7.0 Tesla. *J Vis Exp*. 2021;.
76. Bruschi N, Boffa G, Inglese M. Ultra-high-field 7-T MRI in multiple sclerosis and other demyelinating diseases: from pathology to clinical practice. *Eur Radiol Exp*. 2020;4:59.
77. Wisse LE, Biessels GJ, Heringa SM, et al. Hippocampal subfield volumes at 7T in early Alzheimer's disease and normal aging. *Neurobiol Aging*. 2014;35: 2039–2045.
78. Boutet C, Chupin M, Lehéricy S, et al. Detection of volume loss in hippocampal layers in Alzheimer's disease using 7 T MRI: a feasibility study. *Neuroimage Clin*. 2014;5:341–348.
79. Theysohn JM, Kraff O, Maderwald S, et al. 7 Tesla MRI of microbleeds and white matter lesions as seen in vascular dementia. *J Magn Reson Imaging*. 2011;33:782–791.
80. Brundel M, Heringa SM, de Bresser J, et al. High prevalence of cerebral microbleeds at 7Tesla MRI in patients with early Alzheimer's disease. *J Alzheimers Dis*. 2012;31:259–263.

81. Cosottini M, Frosini D, Pesaresi I, et al. MR imaging of the substantia nigra at 7 T enables diagnosis of Parkinson disease. *Radiology*. 2014;271:831–838.
82. Lehéricy S, Bardinet E, Poupon C, et al. 7 Tesla magnetic resonance imaging: a closer look at substantia nigra anatomy in Parkinson's disease. *Mov Disord*. 2014;29:1574–1581.
83. Kwon DH, Kim JM, Oh SH, et al. Seven-Tesla magnetic resonance images of the substantia nigra in Parkinson disease. *Ann Neurol*. 2012;71:267–277.
84. Cho ZH, Min HK, Oh SH, et al. Direct visualization of deep brain stimulation targets in Parkinson disease with the use of 7-Tesla magnetic resonance imaging. *J Neurosurg*. 2010;113:639–647.
85. van Laar PJ, Oterdoom DL, Ter Horst GJ, et al. Surgical accuracy of 3-Tesla versus 7-Tesla magnetic resonance imaging in deep brain stimulation for Parkinson disease. *World Neurosurg*. 2016;93:410–412.
86. Daghistani R, Widjaja E. Role of MRI in patient selection for surgical treatment of intractable epilepsy in infancy. *Brain Dev*. 2013;35:697–705.
87. De Ciantis A, Barba C, Tassi L, et al. 7T MRI in focal epilepsy with unrevealing conventional field strength imaging. *Epilepsia*. 2016;57:445–454.
88. Wang I, Oh S, Blumcke I, et al. Value of 7T MRI and post-processing in patients with nonlesional 3T MRI undergoing epilepsy presurgical evaluation. *Epilepsia*. 2020;61:2509–2520.
89. Obusez EC, Lowe M, Oh SH, et al. 7T MR of intracranial pathology: preliminary observations and comparisons to 3T and 1.5T. *Neuroimage*. 2018;168: 459–476.
90. Feldman RE, Delman BN, Pawha PS, et al. 7T MRI in epilepsy patients with previously normal clinical MRI exams compared against healthy controls. *PLoS One*. 2019;14:e0213642.
91. Pittau F, Baud MO, Jorge J, et al. MP2RAGE and susceptibility-weighted imaging in lesional epilepsy at 7T. *J Neuroimaging*. 2018;28:365–369.
92. Opheim G, van der Kolk A, Markenroth Bloch K, et al. 7T epilepsy task force consensus recommendations on the use of 7T MRI in clinical practice. *Neurology*. 2021;96:327–341.
93. Canjels LPW, Backes WH, van Veenendaal TM, et al. Volumetric and functional activity lateralization in healthy subjects and patients with focal epilepsy: initial findings in a 7T MRI study. *J Neuroimaging*. 2020;30:666–673.
94. Krug R, Stehling C, Kelley DA, et al. Imaging of the musculoskeletal system in vivo using ultra-high field magnetic resonance at 7 T. *Invest Radiol*. 2009;44: 613–618.
95. Chang G, Pakin SK, Schweitzer ME, et al. Adaptations in trabecular bone microarchitecture in Olympic athletes determined by 7T MRI. *J Magn Reson Imaging*. 2008;27:1089–1095.
96. Chang G, Wang L, Liang G, et al. Reproducibility of subregional trabecular bone micro-architectural measures derived from 7-Tesla magnetic resonance images. *MAGMA*. 2011;24:121–125.
97. Krug R, Han ET, Banerjee S, et al. Fully balanced steady-state 3D-spin-echo (bSSSE) imaging at 3 Tesla. *Magn Reson Med*. 2006;56:1033–1040.
98. Banerjee S, Han ET, Krug R, et al. Application of refocused steady-state free-precession methods at 1.5 and 3 T to in vivo high-resolution MRI of trabecular bone: simulations and experiments. *J Magn Reson Imaging*. 2005;21:818–825.
99. Juras V, Welsch G, Bär P, et al. Comparison of 3T and 7T MRI clinical sequences for ankle imaging. *Eur J Radiol*. 2012;81:1846–1850.
100. Springer E, Bohndorf K, Juras V, et al. Comparison of routine knee magnetic resonance imaging at 3 T and 7 T. *Invest Radiol*. 2017;52:42–54.
101. Treutlein C, Bäuerle T, Nagel AM, et al. Comprehensive assessment of knee joint synovitis at 7T MRI using contrast-enhanced and non-enhanced sequences. *BMC Musculoskelet Disord*. 2020;21:116.
102. Menezes NM, Gray ML, Hartke JR, et al. T2 and T1rho MRI in articular cartilage systems. *Magn Reson Med*. 2004;51:503–509.
103. Lazik A, Theysohn JM, Geis C, et al. 7 Tesla quantitative hip MRI: T1, T2 and T2* mapping of hip cartilage in healthy volunteers. *Eur Radiol*. 2016;26: 1245–1253.
104. Bangerter NK, Taylor MD, Tarbox GJ, et al. Quantitative techniques for musculoskeletal MRI at 7 Tesla. *Quant Imaging Med Surg*. 2016;6:715.
105. Welsch GH, Mamisch TC, Hughes T, et al. In vivo biochemical 7.0 Tesla magnetic resonance: preliminary results of dGEMRIC, zonal T2, and T2* mapping of articular cartilage. *Invest Radiol*. 2008;43:619–626.
106. Raya JG, Horng A, Dietrich O, et al. Articular cartilage: in vivo diffusion-tensor imaging. *Radiology*. 2012;262:550–559.
107. Wyatt C, Guha A, Venkatachari A, et al. Improved differentiation between knees with cartilage lesions and controls using 7T relaxation time mapping. *J Orthop Translat*. 2015;3:197–204.
108. Wei H, Dibb R, Decker K, et al. Investigating magnetic susceptibility of human knee joint at 7 Tesla. *Magn Reson Med*. 2017;78:1933–1943.
109. Wu B, Wang C, Krug R, et al. 7T human spine imaging arrays with adjustable inductive decoupling. *IEEE Trans Biomed Eng*. 2010;57:397–403.
110. Kraff O, Bitz AK, Kruszona S, et al. An eight-channel phased array RF coil for spine MR imaging at 7 T. *Invest Radiol*. 2009;44:734–740.
111. Grams AE, Kraff O, Umutlu L, et al. MRI of the lumbar spine at 7 Tesla in healthy volunteers and a patient with congenital malformations. *Skeletal Radiol*. 2012;41:509–514.
112. Rietsch SHG, Brunheim S, Orzada S, et al. Development and evaluation of a 16-channel receive-only RF coil to improve 7T ultra-high field body MRI with focus on the spine. *Magn Reson Med*. 2019;82:796–810.
113. Massire A, Taso M, Besson P, et al. High-resolution multi-parametric quantitative magnetic resonance imaging of the human cervical spinal cord at 7T. *Neuroimage*. 2016;143:58–69.
114. Massire A, Rasoanandrianina H, Taso M, et al. Feasibility of single-shot multi-level multi-angle diffusion tensor imaging of the human cervical spinal cord at 7T. *Magn Reson Med*. 2018;80:947–957.
115. Lévy S, Roche PH, Guye M, et al. Feasibility of human spinal cord perfusion mapping using dynamic susceptibility contrast imaging at 7T: preliminary results and identified guidelines. *Magn Reson Med*. 2021;85:1183–1194.
116. Galley J, Sutter R, Germann C, et al. High-resolution in vivo MR imaging of intraspinal cervical nerve rootlets at 3 and 7 Tesla. *Eur Radiol*. 2021;31: 4625–4633.
117. Laader A, Beiderwellen K, Kraff O, et al. 1.5 versus 3 versus 7 Tesla in abdominal MRI: a comparative study. *PLoS One*. 2017;12:e0187528.
118. Umutlu L, Orzada S, Kinner S, et al. Renal imaging at 7 Tesla: preliminary results. *Eur Radiol*. 2011;21:841–849.
119. Fischer A, Kraff O, Orzada S, et al. Ultrahigh-field imaging of the biliary tract at 7 T: initial results of gadoxetic acid-enhanced magnetic resonance cholangiography. *Invest Radiol*. 2014;49:346–353.
120. Maas MC, Vos EK, Lagemaat MW, et al. Feasibility of T2 -weighted turbo spin echo imaging of the human prostate at 7 Tesla. *Magn Reson Med*. 2014;71: 1711–1719.
121. Vos EK, Lagemaat MW, Barentsz JO, et al. Image quality and cancer visibility of T2-weighted magnetic resonance imaging of the prostate at 7 Tesla. *Eur Radiol*. 2014;24:1950–1958.
122. Ertürk MA, Tian J, Van de Moortele PF, et al. Development and evaluation of a multichannel endorectal RF coil for prostate MRI at 7T in combination with an external surface array. *J Magn Reson Imaging*. 2016;43:1279–1287.
123. Philips BWJ, Stijns RCH, Rietsch SHG, et al. USPIO-enhanced MRI of pelvic lymph nodes at 7-T: preliminary experience. *Eur Radiol*. 2019;29:6529–6538.
124. Kraff O, Quick HH. 7T: physics, safety, and potential clinical applications. *J Magn Reson Imaging*. 2017;46:1573–1589.
125. Stehouwer BL, Klomp DW, Van Den Bosch MA, et al. Dynamic contrast-enhanced and ultra-high-resolution breast MRI at 7.0 Tesla. *Eur Radiol*. 2013; 23:2961–2968.
126. Bogner W, Pinker K, Zaric O, et al. Bilateral diffusion-weighted MR imaging of breast tumors with submillimeter resolution using readout-segmented echo-planar imaging at 7 T. *Radiology*. 2015;274:74–84.
127. Pinker K, Baltzer P, Bogner W, et al. Multiparametric MR imaging with high-resolution dynamic contrast-enhanced and diffusion-weighted imaging at 7 T improves the assessment of breast tumors: a feasibility study. *Radiology*. 2015;276: 360–370.
128. Schmitz AM, Veldhuis WB, Menke-Pluijmers MB, et al. Multiparametric MRI with dynamic contrast enhancement, diffusion-weighted imaging, and 31-phosphorus spectroscopy at 7 T for characterization of breast cancer. *Invest Radiol*. 2015;50:766–771.
129. Vaughan JT, Snyder CJ, DelaBarre LJ, et al. Whole-body imaging at 7T: preliminary results. *Magn Reson Med*. 2009;61:244–248.
130. Snyder CJ, DelaBarre L, Metzger GJ, et al. Initial results of cardiac imaging at 7 Tesla. *Magn Reson Med*. 2009;61:517–524.
131. von Knobelsdorff-Brenkenhoff F, Tkachenko V, Winter L, et al. Assessment of the right ventricle with cardiovascular magnetic resonance at 7 Tesla. *J Cardiovasc Magn Reson*. 2013;15:23.
132. von Knobelsdorff-Brenkenhoff F, Frauenrath T, Prothmann M, et al. Cardiac chamber quantification using magnetic resonance imaging at 7 Tesla—a pilot study. *Eur Radiol*. 2010;20:2844–2852.
133. Schmitter S, Moeller S, Wu X, et al. Simultaneous multislice imaging in dynamic cardiac MRI at 7T using parallel transmission. *Magn Reson Med*. 2017;77: 1010–1020.
134. Mirkes C, Shajan G, Chadzynski G, et al. (31)P CSI of the human brain in healthy subjects and tumor patients at 9.4 T with a three-layered multi-nuclear coil: initial results. *MAGMA*. 2016;29:579–589.
135. Nagel AM, Amarteifio E, Lehmann-Horn F, et al. 3 Tesla sodium inversion recovery magnetic resonance imaging allows for improved visualization of

intracellular sodium content changes in muscular channelopathies. *Invest Radiol*. 2011;46:759–766.

136. Atkinson IC, Thulborn KR. Feasibility of mapping the tissue mass corrected bioscale of cerebral metabolic rate of oxygen consumption using 17-oxygen and 23-sodium MR imaging in a human brain at 9.4 T. *Neuroimage*. 2010;51:723–733.
137. Niesporek SC, Nagel AM, Platt T. Multinuclear MRI at ultrahigh fields. *Top Magn Reson Imaging*. 2019;28:173–188.
138. United States Food and Drug Administration. 2019. Available at: https://www.accessdata.fda.gov/cdrh_docs/pdf18/K183222.pdf. Accessed June 2021.
139. Henning A. Proton and multinuclear magnetic resonance spectroscopy in the human brain at ultra-high field strength: a review. *Neuroimage*. 2018;168:181–198.
140. Bogner W, Chmelik M, Schmid AI, et al. Assessment of (31)P relaxation times in the human calf muscle: a comparison between 3 T and 7 T in vivo. *Magn Reson Med*. 2009;62:574–582.
141. Lagemaat MW, van de Bank BL, Sati P, et al. Repeatability of (31) P MRSI in the human brain at 7 T with and without the nuclear Overhauser effect. *NMR Biomed*. 2016;29:256–263.
142. Wenger KJ, Hattingen E, Franz K, et al. Intracellular pH measured by $^{31}$ P-MR-spectroscopy might predict site of progression in recurrent glioblastoma under antiangiogenic therapy. *J Magn Reson Imaging*. 2017;46:1200–1208.
143. Maintz D, Heindel W, Kugel H, et al. Phosphorus-31 MR spectroscopy of normal adult human brain and brain tumours. *NMR Biomed*. 2002;15:18–27.
144. Korzowski A, Weinfurtner N, Mueller S, et al. Volumetric mapping of intra- and extracellular pH in the human brain using $^{31}$ P MRSI at 7T. *Magn Reson Med*. 2020;84:1707–1723.
145. Valkovič L, Chmelík M, Kršňák M. In-vivo$^{31}$P-MRS of skeletal muscle and liver: a way for non-invasive assessment of their metabolism. *Anal Biochem*. 2017;529:193–215.
146. Lei H, Zhu XH, Zhang XL, et al. In vivo 31P magnetic resonance spectroscopy of human brain at 7 T: an initial experience. *Magn Reson Med*. 2003;49:199–205.
147. Zhu XH, Qiao H, Du F, et al. Quantitative imaging of energy expenditure in human brain. *Neuroimage*. 2012;60:2107–2117.
148. Ren J, Sherry AD, Malloy CR. Efficient (31) P band inversion transfer approach for measuring creatine kinase activity, ATP synthesis, and molecular dynamics in the human brain at 7 T. *Magn Reson Med*. 2017;78:1657–1666.
149. Zhu XH, Lu M, Lee BY, et al. In vivo NAD assay reveals the intracellular NAD contents and redox state in healthy human brain and their age dependences. *Proc Natl Acad Sci U S A*. 2015;112:2876–2881.
150. Loring J, van der Kemp WJM, Almujayyaz S, et al. Whole-body radiofrequency coil for (31) P MRSI at 7 T. *NMR Biomed*. 2016;29:709–720.
151. Valkovic L, Dragonu I, Almujayyaz S, et al. Using a whole-body 31P birdcage transmit coil and 16-element receive array for human cardiac metabolic imaging at 7 T. *PLoS One*. 2017;12:e0187153.
152. van Houtum Q, Welting D, Gosselink WJM, et al. Low SAR (31) P (multi-echo) spectroscopic imaging using an integrated whole-body transmit coil at 7 T. *NMR Biomed*. 2019;32:e4178.
153. Luttje MP, Italiaander MGM, Arteaga de Castro CS, et al. (31) P MR spectroscopic imaging combined with (1) H MR spectroscopic imaging in the human prostate using a double tuned endorectal coil at 7 T. *Magn Reson Med*. 2014;72:1516–1521.
154. van der Velden TA, Italiaander M, van der Kemp WJM, et al. Radiofrequency configuration to facilitate bilateral breast (31) P MR spectroscopic imaging and high-resolution MRI at 7 Tesla. *Magn Reson Med*. 2015;74:1803–1810.
155. Goluch S, Kuehne A, Meyerspeer M, et al. A form-fitted three channel (31) P, two channel (1) H transceiver coil array for calf muscle studies at 7 T. *Magn Reson Med*. 2015;73:2376–2389.
156. Rodgers CT, Clarke WT, Snyder C, et al. Human cardiac 31P magnetic resonance spectroscopy at 7 Tesla. *Magn Reson Med*. 2014;72:304–315.
157. Hattingen E, Magerkurth J, Pilatus U, et al. Phosphorus and proton magnetic resonance spectroscopy demonstrates mitochondrial dysfunction in early and advanced Parkinson's disease. *Brain*. 2009;132:3285–3297.
158. Rango M, Bonifati C, Bresolin N. Parkinson's disease and brain mitochondrial dysfunction: a functional phosphorus magnetic resonance spectroscopy study. *J Cereb Blood Flow Metab*. 2006;26:283–390.
159. Montagna P, Pierangeli G, Cortelli P, et al. Brain oxidative metabolism in Parkinson's disease studied by phosphorus 31 magnetic resonance spectroscopy. *J Neuroimaging*. 1993;3. doi:10.1111/jon199334225.
160. Brockmann K, Hilker R, Pilatus U, et al. GBA-associated PD. Neurodegeneration, altered membrane metabolism, and lack of energy failure. *Neurology*. 2012;79:213–220.
161. Hu MT, Taylor-Robinson SD, Chaudhuri KR, et al. Cortical dysfunction in non-demented Parkinson's disease patients: a combined (31)P-MRS and (18)FDG-PET study. *Brain*. 2000;123:340–352.
162. Weiduschat N, Mao X, Beal MF, et al. Usefulness of proton and phosphorus MR spectroscopic imaging for early diagnosis of Parkinson's disease. *J Neuroimaging*. 2015;25:105–110.
163. Barbiroli B, Martinelli P, Patuelli A, et al. Phosphorus magnetic resonance spectroscopy in multiple system atrophy and Parkinson's disease. *Mov Disord*. 1999;14:430–435.
164. Rijpma A, van der Graaf M, Meulenbroek O, et al. Altered brain high-energy phosphate metabolism in mild Alzheimer's disease: a 3-dimensional (31)P MR spectroscopic imaging study. *Neuroimage Clin*. 2018;18:254–261.
165. Pan JW, Williamson A, Cavus I, et al. Neurometabolism in human epilepsy. *Epilepsia*. 2008;49:31–41.
166. van der Grond J, Gerson JR, Laxer KD, et al. Regional distribution of interictal 31P metabolic changes in patients with temporal lobe epilepsy. *Epilepsia*. 1998;39:527–536.
167. Zhu XH, Lee BY, Tuite P, et al. Quantitative assessment of occipital metabolic and energetic changes in Parkinson's patients, using in vivo (31)P MRS-based metabolic imaging at 7 T. *Metabolites*. 2021;11:145.
168. Chmelik M, Povazan M, Krssak M, et al. In vivo (31)P magnetic resonance spectroscopy of the human liver at 7 T: an initial experience. *NMR Biomed*. 2014;27:478–485.
169. Chmelik M, Valkovic L, Wolf P, et al. Phosphatidylcholine contributes to in vivo (31)P MRS signal from the human liver. *Eur Radiol*. 2015;25:2059–2066.
170. Gajdosik M, Chadzynski GL, Hangel G, et al. Ultrashort-TE stimulated echo acquisition mode (STEAM) improves the quantification of lipids and fatty acid chain unsaturation in the human liver at 7 T. *NMR Biomed*. 2015;28:1283–1293.
171. Purvis LAB, Clarke WT, Valkovic L, et al. Phosphodiester content measured in human liver by in vivo (31) P MR spectroscopy at 7 Tesla. *Magn Reson Med*. 2017;78:2095–2105.
172. Klomp DWJ, van de Bank BL, Raaijmakers A, et al. 31P MRSI and 1H MRS at 7 T: initial results in human breast cancer. *NMR Biomed*. 2011;24:1337–1342.
173. van Houtum QQ, Mohamed Hoesein FFAA, Verhoeff JJJC, et al. Feasibility of (31) P spectroscopic imaging at 7 T in lung carcinoma patients. *NMR Biomed*. 2021;34:e4204.
174. Parasoglou P, Xia D, Chang G, et al. Dynamic three-dimensional imaging of phosphocreatine recovery kinetics in the human lower leg muscles at 3T and 7T: a preliminary study. *NMR Biomed*. 2013;26:348–356.
175. Madelin G, Regatte RR. Biomedical applications of sodium MRI in vivo. *J Magn Reson Imaging*. 2013;38:511–529.
176. Staroswiecki E, Bangerter NK, Gurney PT, et al. In vivo sodium imaging of human patellar cartilage with a 3D cones sequence at 3 T and 7 T. *J Magn Reson Imaging*. 2010;32:446–451.
177. Platt T, Umathum R, Fiedler TM, et al. In vivo self-gated $^{23}$Na MRI at 7 T using an oval-shaped body resonator. *Magn Reson Med*. 2018;80:1005–1019.
178. Wetterling F, Corteville DM, Kalayciyan R, et al. Whole body sodium MRI at 3T using an asymmetric birdcage resonator and short echo time sequence: first images of a male volunteer. *Phys Med Biol*. 2012;57:4555–4567.
179. Graessl A, Ruehle A, Waiczies H, et al. Sodium MRI of the human heart at 7.0 T: preliminary results. *NMR Biomed*. 2015;28:967–975.
180. Kaggie JD, Hadley JR, Badal J, et al. A 3 T sodium and proton composite array breast coil. *Magn Reson Med*. 2014;71:2231–2242.
181. Bottomley PA. Sodium MRI in human heart: a review. *NMR Biomed*. 2016;29:187–196.
182. Ouwerkerk R, Jacobs MA, Macura KJ, et al. Elevated tissue sodium concentration in malignant breast lesions detected with non-invasive 23Na MRI. *Breast Cancer Res Treat*. 2007;106:151–160.
183. Zollner FG, Konstandin S, Lommen J, et al. Quantitative sodium MRI of kidney. *NMR Biomed*. 2016;29:197–205.
184. Lott J, Platt T, Niesporek SC, et al. Corrections of myocardial tissue sodium concentration measurements in human cardiac $^{23}$Na MRI at 7 Tesla. *Magn Reson Med*. 2019;82:159–173.
185. Huhn K, Engelhorn T, Linker RA, et al. Potential of sodium MRI as a biomarker for neurodegeneration and neuroinflammation in multiple sclerosis. *Front Neurol*. 2019;10:84.
186. Inglese M, Madelin G, Oesingmann N, et al. Brain tissue sodium concentration in multiple sclerosis: a sodium imaging study at 3 Tesla. *Brain*. 2010;133:847–857.
187. Petracca M, Vancea RO, Fleysher L, et al. Brain intra- and extracellular sodium concentration in multiple sclerosis: a 7 T MRI study. *Brain*. 2016;139:795–806.
188. Zaaraoui W, Konstandin S, Audoin B, et al. Distribution of brain sodium accumulation correlates with disability in multiple sclerosis: a cross-sectional 23Na MR imaging study. *Radiology*. 2012;264:859–867.

189. Paling D, Solanky BS, Riemer F, et al. Sodium accumulation is associated with disability and a progressive course in multiple sclerosis. *Brain*. 2013;136:2305–2317.
190. Maarouf A, Audoin B, Pariollaud F, et al. Increased total sodium concentration in gray matter better explains cognition than atrophy in MS. *Neurology*. 2017;88:289–295.
191. Eisele P, Konstandin S, Szabo K, et al. Temporal evolution of acute multiple sclerosis lesions on serial sodium ($^{23}$Na) MRI. *Mult Scler Relat Disord*. 2019;29:48–54.
192. Maarouf A, Audoin B, Konstandin S, et al. Topography of brain sodium accumulation in progressive multiple sclerosis. *MAGMA*. 2014;27:53–62.
193. Grist JT, Riemer F, McLean MA, et al. Imaging intralesional heterogeneity of sodium concentration in multiple sclerosis: initial evidence from $^{23}$Na-MRI. *J Neurol Sci*. 2018;387:111–114.
194. Huhn K, Mennecke A, Linz P, et al. $^{23}$Na MRI reveals persistent sodium accumulation in tumefactive MS lesions. *J Neurol Sci*. 2017;379:163–616.
195. Fleysher L, Oesingmann N, Inglese M. $B_0$ inhomogeneity-insensitive triple-quantum-filtered sodium imaging using a 12-step phase-cycling scheme. *NMR Biomed*. 2010;23:1191–1198.
196. Reetz K, Romanzetti S, Dogan I, et al. Increased brain tissue sodium concentration in Huntington's disease—a sodium imaging study at 4 T. *Neuroimage*. 2012;63:517–524.
197. Mellon EA, Pilkinton DT, Clark CM, et al. Sodium MR imaging detection of mild Alzheimer disease: preliminary study. *AJNR Am J Neuroradiol*. 2009;30:978–984.
198. Shimizu T, Naritomi H, Sawada T. Sequential changes on 23Na MRI after cerebral infarction. *Neuroradiology*. 1993;35:416–419.
199. Meyer MM, Schmidt A, Benrath J, et al. Cerebral sodium ($^{23}$Na) magnetic resonance imaging in patients with migraine—a case-control study. *Eur Radiol*. 2019;29:7055–7062.
200. Ridley B, Marchi A, Wirsich J, et al. Brain sodium MRI in human epilepsy: disturbances of ionic homeostasis reflect the organization of pathological regions. *Neuroimage*. 2017;157:173–183.
201. Thulborn KR, Davis D, Adams H, et al. Quantitative tissue sodium concentration mapping of the growth of focal cerebral tumors with sodium magnetic resonance imaging. *Magn Reson Med*. 1999;41:351–359.
202. Ouwerkerk R, Bleich KB, Gillen JS, et al. Tissue sodium concentration in human brain tumors as measured with 23Na MR imaging. *Radiology*. 2003;227:529–537.
203. Boada FE, Tanase C, Davis D, et al. Non-invasive assessment of tumor proliferation using triple quantum filtered 23/Na MRI: technical challenges and solutions. *Conf Proc IEEE Eng Med Biol Soc*. 2004;2004:5238–5241.
204. Laymon CM, Oborski MJ, Lee VK, et al. Combined imaging biomarkers for therapy evaluation in glioblastoma multiforme: correlating sodium MRI and F-18 FLT PET on a voxel-wise basis. *Magn Reson Imaging*. 2012;30:1268–1278.
205. Regnery S, Behl NGR, Platt T, et al. Ultra-high-field sodium MRI as biomarker for tumor extent, grade and IDH mutation status in glioma patients. *Neuroimage Clin*. 2020;28:102427.
206. Zbyn S, Mlynarik V, Juras V, et al. Evaluation of cartilage repair and osteoarthritis with sodium MRI. *NMR Biomed*. 2016;29:206–215.
207. Gerhalter T, Gast LV, Marty B, et al. $^{23}$Na MRI depicts early changes in ion homeostasis in skeletal muscle tissue of patients with Duchenne muscular dystrophy. *J Magn Reson Imaging*. 2019;50:1103–1113.
208. Weber MA, Nagel AM, Jurkat-Rott K, et al. Sodium (23Na) MRI detects elevated muscular sodium concentration in Duchenne muscular dystrophy. *Neurology*. 2011;77:2017–2024.
209. Dahlmann A, Dorfelt K, Eicher F, et al. Magnetic resonance-determined sodium removal from tissue stores in hemodialysis patients. *Kidney Int*. 2015;87:434–441.
210. Kopp C, Linz P, Maier C, et al. Elevated tissue sodium deposition in patients with type 2 diabetes on hemodialysis detected by $^{23}$Na magnetic resonance imaging. *Kidney Int*. 2018;93:1191–1197.
211. Chang G, Wang L, Schweitzer ME, et al. 3D 23Na MRI of human skeletal muscle at 7 Tesla: initial experience. *Eur Radiol*. 2010;20:2039–2046.
212. Weber MA, Nagel AM, Marschar AM, et al. 7-T (35)Cl and (23)Na MR imaging for detection of mutation-dependent alterations in muscular edema and fat fraction with sodium and chloride concentrations in muscular periodic paralyses. *Radiology*. 2016;280:848–859.
213. Sandstede JJ, Hillenbrand H, Beer M, et al. Time course of 23Na signal intensity after myocardial infarction in humans. *Magn Reson Med*. 2004;52:545–551.
214. Constantinides CD, Kraitchman DL, O'Brien KO, et al. Noninvasive quantification of total sodium concentrations in acute reperfused myocardial infarction using 23Na MRI. *Magn Reson Med*. 2001;46:1144–1151.
215. Haneder S, Konstandin S, Morelli JN, et al. Quantitative and qualitative $^{23}$Na MR imaging of the human kidneys at 3 T: before and after a water load. *Radiology*. 2011;260:857–865.
216. Haneder S, Konstandin S, Morelli JN, et al. Assessment of the renal corticomedullary (23)Na gradient using isotropic data sets. *Acad Radiol*. 2013;20:407–413.
217. Moon CH, Furlan A, Kim JH, et al. Quantitative sodium MR imaging of native versus transplanted kidneys using a dual-tuned proton/sodium (1H/ 23Na) coil: initial experience. *Eur Radiol*. 2014;24:1320–1326.
218. Rosen Y, Lenkinski RE. Sodium MRI of a human transplanted kidney. *Acad Radiol*. 2009;16:886–889.
219. Haneder S, Juras V, Michaely HJ, et al. In vivo sodium (23Na) imaging of the human kidneys at 7 T: preliminary results. *Eur Radiol*. 2014;24:494–501.
220. Maril N, Rosen Y, Reynolds GH, et al. Sodium MRI of the human kidney at 3 Tesla. *Magn Reson Med*. 2006;56:1229–1234.
221. Zaric O, Pinker K, Zbyn S, et al. Quantitative sodium MR imaging at 7 T: initial results and comparison with diffusion-weighted imaging in patients with breast tumors. *Radiology*. 2016;280:39–48.
222. Zaric O, Farr A, Minarikova L, et al. Tissue sodium concentration quantification at 7.0-T MRI as an early marker for chemotherapy response in breast cancer: a feasibility study. *Radiology*. 2021;299:63–72.
223. Henzler T, Konstandin S, Schmid-Bindert G, et al. Imaging of tumor viability in lung cancer: initial results using 23Na-MRI. *Rofo*. 2012;184:340–344.
224. Hausmann D, Konstandin S, Wetterling F, et al. Apparent diffusion coefficient and sodium concentration measurements in human prostate tissue via hydrogen-1 and sodium-23 magnetic resonance imaging in a clinical setting at 3T. *Invest Radiol*. 2012;47:677–682.
225. Nagel AM, Lehmann-Horn F, Weber MA, et al. In vivo 35Cl MR imaging in humans: a feasibility study. *Radiology*. 2014;271:585–595.
226. Niesporek SC, Umathum R, Fiedler TM, et al. Improved T*(2) determination in $^{23}$Na, $^{35}$Cl, and $^{17}$O MRI using iterative partial volume correction based on $^{1}$H MRI segmentation. *MAGMA*. 2017;30:519–536.
227. Umathum R, Rosler MB, Nagel AM. In vivo 39K MR imaging of human muscle and brain. *Radiology*. 2013;269:569–576.
228. Atkinson IC, Claiborne TC, Thulborn KR. Feasibility of 39-potassium MR imaging of a human brain at 9.4 Tesla. *Magn Reson Med*. 2014;71:1819–1825.
229. Gast LV, Volker S, Utzschneider M, et al. Combined imaging of potassium and sodium in human skeletal muscle tissue at 7 T. *Magn Reson Med*. 2021;85:239–253.
230. Wenz D, Nagel AM, Lott J, et al. In vivo potassium MRI of the human heart. *Magn Reson Med*. 2020;83:203–213.
231. Niesporek SC, Umathum R, Lommen JM, et al. Reproducibility of $CMRO_2$ determination using dynamic $^{17}$O MRI. *Magn Reson Med*. 2018;79:2923–2934.
232. Hoffmann SH, Radbruch A, Bock M, et al. Direct (17)O MRI with partial volume correction: first experiences in a glioblastoma patient. *MAGMA*. 2014;27:579–587.
233. Paech D, Nagel AM, Schultheiss MN, et al. Quantitative dynamic oxygen 17 MRI at 7.0 T for the cerebral oxygen metabolism in glioma. *Radiology*. 2020;295:181–189.
234. De Feyter HM, Behar KL, Corbin ZA, et al. Deuterium metabolic imaging (DMI) for MRI-based 3D mapping of metabolism in vivo. *Sci Adv*. 2018;4:eaat7314.
235. De Feyter HM, Thomas MA, Behar KL, et al. NMR visibility of deuterium-labeled liver glycogen in vivo. *Magn Reson Med*. 2021;86:62–68.
236. Hesse F, Somai V, Kreis F, et al. Monitoring tumor cell death in murine tumor models using deuterium magnetic resonance spectroscopy and spectroscopic imaging. *Proc Natl Acad Sci U S A*. 2021;118:e2014631118.
237. Kreis F, Wright AJ, Hesse F, et al. Measuring tumor glycolytic flux in vivo by using fast deuterium MRI. *Radiology*. 2020;294:289–296.
238. Riis-Vestergaard MJ, Laustsen C, Mariager CØ, et al. Glucose metabolism in brown adipose tissue determined by deuterium metabolic imaging in rats. *Int J Obes (Lond)*. 2020;44:1417–1427.
239. Lu M, Zhu XH, Zhang Y, et al. Quantitative assessment of brain glucose metabolic rates using in vivo deuterium magnetic resonance spectroscopy. *J Cereb Blood Flow Metab*. 2017;37:3518–3530.
240. De Feyter HM, de Graaf RA. Deuterium metabolic imaging—back to the future. *J Magn Reson*. 2021;326:106932.
241. Straathof M, Meerwaldt AE, De Feyter HM, et al. Deuterium metabolic imaging of the healthy and diseased brain. *Neuroscience*. 2021;S0306-4522(21)00030-0.
242. de Graaf RA, Hendriks AD, Klomp DWJ, et al. On the magnetic field dependence of deuterium metabolic imaging. *NMR Biomed*. 2020;33:e4235.
243. Zwingmann C, Leibfritz D. Regulation of glial metabolism studied by 13C-NMR. *NMR Biomed*. 2003;16:370–399.

244. Garcia-Espinosa MA, Rodrigues TB, Sierra A, et al. Cerebral glucose metabolism and the glutamine cycle as detected by in vivo and in vitro 13C NMR spectroscopy. *Neurochem Int*. 2004;45:297–303.
245. Goluch S, Frass-Kriegl R, Meyerspeer M, et al. Proton-decoupled carbon magnetic resonance spectroscopy in human calf muscles at 7 T using a multichannel radiofrequency coil. *Sci Rep*. 2018;8:6211.
246. Heinicke K, Dimitrov IE, Romain N, et al. Reproducibility and absolute quantification of muscle glycogen in patients with glycogen storage disease by 13C NMR spectroscopy at 7 Tesla. *PLoS One*. 2014;9:e108706.
247. Chen J, Lanza GM, Wickline SA. Quantitative magnetic resonance fluorine imaging: today and tomorrow. *Wiley Interdiscip Rev Nanomed Nanobiotechnol*. 2010;2:431–440.
248. Jacoby C, Borg N, Heusch P, et al. Visualization of immune cell infiltration in experimental viral myocarditis by (19)F MRI in vivo. *MAGMA*. 2014;27:101–106.
249. Ghuman H, Hitchens TK, Modo M. A systematic optimization of (19)F MR image acquisition to detect macrophage invasion into an ECM hydrogel implanted in the stroke-damaged brain. *Neuroimage*. 2019;202:116090.
250. Deelchand DK, Van de Moortele PF, Adriany G, et al. In vivo 1H NMR spectroscopy of the human brain at 9.4 T: initial results. *J Magn Reson*. 2010;206:74–80.
251. Mlynarik V, Gambarota G, Frenkel H, et al. Localized short-echo-time proton MR spectroscopy with full signal-intensity acquisition. *Magn Reson Med*. 2006;56:965–970.
252. Boer VO, van Lier AL, Hoogduin JM, et al. 7-T (1) H MRS with adiabatic refocusing at short TE using radiofrequency focusing with a dual-channel volume transmit coil. *NMR Biomed*. 2011;24:1038–1046.
253. Fuchs A, Luttje M, Boesiger P, et al. SPECIAL semi-LASER with lipid artifact compensation for 1H MRS at 7 T. *Magn Reson Med*. 2013;69:603–612.
254. Nassirpour S, Chang P, Fillmer A, et al. A comparison of optimization algorithms for localized in vivo B0 shimming. *Magn Reson Med*. 2018;79:1145–1156.
255. Tkac I, Gruetter R. Methodology of H NMR spectroscopy of the human brain at very high magnetic fields. *Appl Magn Reson*. 2005;29:139–157.
256. Andronesi OC, Bhattacharyya PK, Bogner W, et al. Motion correction methods for MRS: experts' consensus recommendations. *NMR Biomed*. 2021;34:e4364.
257. Mekle R, Mlynárik V, Gambarota G, et al. MR spectroscopy of the human brain with enhanced signal intensity at ultrashort echo times on a clinical platform at 3 T and 7 T. *Magn Reson Med*. 2009;61:1279–1285.
258. Louis DN, Perry A, Reifenberger G, et al. The 2016 World Health Organization classification of tumors of the central nervous system: a summary. *Acta Neuropathol*. 2016;131:803–820.
259. Pope WB, Prins RM, Albert Thomas M, et al. Non-invasive detection of 2-hydroxyglutarate and other metabolites in *IDH1* mutant glioma patients using magnetic resonance spectroscopy. *J Neurooncol*. 2012;107:197–205.
260. Emir UE, Larkin SJ, de Pennington N, et al. Noninvasive quantification of 2-hydroxyglutarate in human gliomas with *IDH1* and *IDH2* mutations. *Cancer Res*. 2016;76:43–49.
261. Prinsen H, de Graaf RA, Mason GF, et al. Reproducibility measurement of glutathione, GABA, and glutamate: towards in vivo neurochemical profiling of multiple sclerosis with MR spectroscopy at 7 T. *J Magn Reson Imaging*. 2017;45:187–198.
262. Atassi N, Xu M, Triantafyllou C, et al. Ultra high-field (7tesla) magnetic resonance spectroscopy in amyotrophic lateral sclerosis. *PLoS One*. 2017;12:e0177680.
263. van den Bogaard SJA, Dumas EM, Teeuwisse WM, et al. Exploratory 7-Tesla magnetic resonance spectroscopy in Huntington's disease provides in vivo evidence for impaired energy metabolism. *J Neurol*. 2011;258:2230–2239.
264. Oeltzschner G, Wijtenburg SA, Mikkelsen M, et al. Neurometabolites and associations with cognitive deficits in mild cognitive impairment: a magnetic resonance spectroscopy study at 7 Tesla. *Neurobiol Aging*. 2019;73:211–218.
265. Henning A, Fuchs A, Murdoch JB, et al. Slice-selective FID acquisition, localized by outer volume suppression (FIDLOVS) for 1H-MRSI of the human brain at 7 T with minimal signal loss. *NMR Biomed*. 2009;22:683–696.
266. Bogner W, Gruber S, Trattnig S, et al. High-resolution mapping of human brain metabolites by free induction decay 1H MRSI at 7 T. *NMR Biomed*. 2012;25:873–882.
267. Gruber S, Heckova E, Strasser B, et al. Mapping an extended neurochemical profile at 3 and 7 T using accelerated high-resolution proton magnetic resonance spectroscopic imaging. *Invest Radiol*. 2017;52:631–639.
268. Nassirpour S, Chang P, Kirchner T, et al. Over-discretized SENSE reconstruction and B0 correction for accelerated non-lipid-suppressed 1H FID MRSI of the human brain at 9.4 T. *NMR Biomed*. 2018;31:e4014.
269. Strasser B, Považan M, Hangel G, et al. (2 + 1)D-CAIPIRINHA accelerated MR spectroscopic imaging of the brain at 7T. *Magn Reson Med*. 2017;78:429–440.
270. Hingerl L, Bogner W, Moser P, et al. Density-weighted concentric circle trajectories for high resolution brain magnetic resonance spectroscopic imaging at 7T. *Magn Reson Med*. 2018;79:2874–2885.
271. Hingerl L, Strasser B, Moser P, et al. Clinical high-resolution 3D-MR spectroscopic imaging of the human brain at 7 T. *Invest Radiol*. 2020;55:239–248.
272. Hangel G, Jain S, Springer E, et al. High-resolution metabolic mapping of gliomas via patch-based super-resolution magnetic resonance spectroscopic imaging at 7 T. *Neuroimage*. 2019;191:587–595.
273. Bogner W, Gagoski B, Hess AT, et al. 3D GABA imaging with real-time motion correction, shim update and reacquisition of adiabatic spiral MRSI. *Neuroimage*. 2014;103:290–302.
274. Andronesi OC, Loebel F, Bogner W, et al. Treatment response assessment in IDH-mutant glioma patients by noninvasive 3D functional spectroscopic mapping of 2-hydroxyglutarate. *Clin Cancer Res*. 2016;22:1632–1641.
275. Ramadan S, Ratai E-M, Wald LL, et al. In vivo 1D and 2D correlation MR spectroscopy of the soleus muscle at 7T. *J Magn Reson*. 2010;204:91–98.
276. Khuu A, Ren J, Dimitrov I, et al. Orientation of lipid strands in the extracellular compartment of muscle: effect on quantitation of intramyocellular lipids. *Magn Reson Med*. 2009;61:16–21.
277. Lagemaat MW, Breukels V, Vos EK, et al. (1)H MR spectroscopic imaging of the prostate at 7T using spectral-spatial pulses. *Magn Reson Med*. 2016;75:933–945.
278. Korteweg MA, Veldhuis WB, Visser F, et al. Feasibility of 7 Tesla breast magnetic resonance imaging determination of intrinsic sensitivity and high-resolution magnetic resonance imaging, diffusion-weighted imaging, and 1H-magnetic resonance spectroscopy of breast cancer patients receiving neoadjuvant therapy. *Invest Radiol*. 2011;46:370–376.
279. Thulborn KR, Waterton JC, Matthews PM, et al. Oxygenation dependence of the transverse relaxation time of water protons in whole blood at high field. *Biochim Biophys Acta*. 1982;714:265–270.
280. Ogawa S, Lee TM, Kay AR, et al. Brain magnetic resonance imaging with contrast dependent on blood oxygenation. *Proc Natl Acad Sci U S A*. 1990;87:9868–9872.
281. Ogawa S, Tank DW, Menon R, et al. Intrinsic signal changes accompanying sensory stimulation: functional brain mapping with magnetic resonance imaging. *Proc Natl Acad Sci*. 1992;89:5951–5955.
282. Olman CA, Van de Moortele PF, Schumacher JF, et al. Retinotopic mapping with spin echo BOLD at 7T. *Magn Reson Imaging*. 2010;28:1258–1269.
283. van der Zwaag W, Francis S, Head K, et al. fMRI at 1.5, 3 and 7 T: characterising BOLD signal changes. *Neuroimage*. 2009;47:1425–1434.
284. Ogawa S, Menon RS, Tank DW, et al. Functional brain mapping by blood oxygenation level-dependent contrast magnetic resonance imaging. A comparison of signal characteristics with a biophysical model. *Biophys J*. 1993;64:803–812.
285. Lee SP, Silva AC, Ugurbil K, et al. Diffusion-weighted spin-echo fMRI at 9.4 T: microvascular/tissue contribution to BOLD signal changes. *Magn Reson Med*. 1999;42:919–928.
286. Ugurbil K. Magnetic resonance imaging at ultrahigh fields. *IEEE Trans Biomed Eng*. 2014;61:1364–1379.
287. Yacoub E, Grier MD, Auerbach EJ, et al. Ultra-high field (10.5 T) resting state fMRI in the macaque. *Neuroimage*. 2020;223:117349.
288. Marques JP, Norris DG. How to choose the right MR sequence for your research question at 7T and above? *Neuroimage*. 2018;168:119–140.
289. Duyn JH. The future of ultra-high field MRI and fMRI for study of the human brain. *Neuroimage*. 2012;62:1241–1248.
290. Heidemann RM, Ivanov D, Trampel R, et al. Isotropic submillimeter fMRI in the human brain at 7 T: combining reduced field-of-view imaging and partially parallel acquisitions. *Magn Reson Med*. 2012;68:1506–1516.
291. Formisano E, Kim DS, Di Salle F, et al. Mirror-symmetric tonotopic maps in human primary auditory cortex. *Neuron*. 2003;40:859–869.
292. Sanchez-Panchuelo RM, Besle J, Beckett A, et al. Within-digit functional parcellation of Brodmann areas of the human primary somatosensory cortex using functional magnetic resonance imaging at 7 Tesla. *J Neurosci*. 2012;32:15815–15822.
293. Marques JP, van der Zwaag W, Granziera C, et al. Cerebellar cortical layers: in vivo visualization with structural high-field-strength MR imaging. *Radiology*. 2010;254:942–948.
294. Boillat Y, Bazin PL, van der Zwaag W. Whole-body somatotopic maps in the cerebellum revealed with 7T fMRI. *Neuroimage*. 2020;211:116624.
295. Thomas BP, Welch EB, Niederhauser BD, et al. High-resolution 7T MRI of the human hippocampus in vivo. *J Magn Reson Imaging*. 2008;28:1266–1272.
296. Solano-Castiella E, Schafer A, Reimer E, et al. Parcellation of human amygdala in vivo using ultra high field structural MRI. *Neuroimage*. 2011;58:741–748.
297. Beisteiner R, Robinson S, Wurnig M, et al. Clinical fMRI: evidence for a 7 T benefit over 3 T. *Neuroimage*. 2011;57:1015–1021.

298. Nasr S, Polimeni JR, Tootell RB. Interdigitated color- and disparity-selective columns within human visual cortical areas V2 and V3. *J Neurosci*. 2016;36:1841–1857.

299. Yacoub E, Harel N, Ugurbil K. High-field fMRI unveils orientation columns in humans. *Proc Natl Acad Sci U S A*. 2008;105:10607–10612.

300. Markuerkiaga I, Marques JP, Gallagher TE, et al. Estimation of laminar BOLD activation profiles using deconvolution with a physiological point spread function. *J Neurosci Methods*. 2021;353:109095.

301. Koopmans PJ, Barth M, Norris DG. Layer-specific BOLD activation in human V1. *Hum Brain Mapp*. 2010;31:1297–1304.

302. Yacoub E, Shmuel A, Logothetis N, et al. Robust detection of ocular dominance columns in humans using Hahn spin echo BOLD functional MRI at 7 Tesla. *Neuroimage*. 2007;37:1161–1177.

303. Lima Cardoso P, Fischmeister FPS, Dymerska B, et al. Robust presurgical functional MRI at 7 T using response consistency. *Hum Brain Mapp*. 2017;38:3163–3174.

304. Dymerska B, Cardoso PDL, Bachrata B, et al. The impact of echo time shifts and temporal signal fluctuations on BOLD sensitivity in presurgical planning at 7 T. *Invest Radiol*. 2019;54:340–348.

305. Ward KM, Aletras AH, Balaban RS. A new class of contrast agents for MRI based on proton chemical exchange dependent saturation transfer (CEST). *J Magn Reson*. 2000;143:79–87.

306. Zhou J, Payen J-F, Wilson DA, et al. Using the amide proton signals of intracellular proteins and peptides to detect pH effects in MRI. *Nat Med*. 2003;9:1085–1090.

307. Paech D, Schlemmer HP. Clinical MR biomarkers. *Recent Results Cancer Res*. 2020;216:719–745.

308. Jones CK, Huang A, Xu J, et al. Nuclear Overhauser enhancement (NOE) imaging in the human brain at 7T. *Neuroimage*. 2013;77:114–124.

309. Zaiss M, Windschuh J, Paech D, et al. Relaxation-compensated CEST-MRI of the human brain at 7T: unbiased insight into NOE and amide signal changes in human glioblastoma. *Neuroimage*. 2015;112:180–188.

310. Zaiß M, Schmitt B, Bachert P. Quantitative separation of CEST effect from magnetization transfer and spillover effects by Lorentzian-line-fit analysis of z-spectra. *J Magn Reson*. 2011;211:149–155.

311. Zaiss M, Xu J, Goerke S, et al. Inverse Z-spectrum analysis for spillover-, MT-, and T1 -corrected steady-state pulsed CEST-MRI—application to pH-weighted MRI of acute stroke. *NMR Biomed*. 2014;27:240–252.

312. Zaiss M, Windschuh J, Goerke S, et al. Downfield-NOE-suppressed amide-CEST-MRI at 7 Tesla provides a unique contrast in human glioblastoma. *Magn Reson Med*. 2016;77:196–208.

313. Zaiss M, Ehses P, Scheffler K. Snapshot-CEST: optimizing spiral-centric-reordered gradient echo acquisition for fast and robust 3D CEST MRI at 9.4 T. *NMR Biomed*. 2018;31:e3879.

314. Park KJ, Kim HS, Park JE, et al. Added value of amide proton transfer imaging to conventional and perfusion MR imaging for evaluating the treatment response of newly diagnosed glioblastoma. *Eur Radiol*. 2016;26:4390–4403.

315. Park JE, Kim HS, Park KJ, et al. Pre- and Posttreatment glioma: comparison of amide proton transfer imaging with MR spectroscopy for biomarkers of tumor proliferation. *Radiology*. 2016;278:514–523.

316. Mehrabian H, Myrehaug S, Soliman H, et al. Evaluation of glioblastoma response to therapy with chemical exchange saturation transfer. *Int J Radiat Oncol Biol Phys*. 2018;101:713–723.

317. Park JE, Kim HS, Park SY, et al. Identification of early response to anti-angiogenic therapy in recurrent glioblastoma: amide proton transfer-weighted and perfusion-weighted MRI compared with diffusion-weighted MRI. *Radiology*. 2020;295:397–406.

318. Regnery S, Adeberg S, Dreher C, et al. Chemical exchange saturation transfer MRI serves as predictor of early progression in glioblastoma patients. *Oncotarget*. 2018;9:28772–28783.

319. Paech D, Dreher C, Regnery S, et al. Relaxation-compensated amide proton transfer (APT) MRI signal intensity is associated with survival and progression in high-grade glioma patients. *Eur Radiol*. 2019;29:4957–4967.

320. Togao O, Yoshiura T, Keupp J, et al. Amide proton transfer imaging of adult diffuse gliomas: correlation with histopathological grades. *Neuro Oncol*. 2014;16:441–448.

321. Bai Y, Lin Y, Zhang W, et al. Noninvasive amide proton transfer magnetic resonance imaging in evaluating the grading and cellularity of gliomas. *Oncotarget*. 2017;8:5834–5842.

322. Sakata A, Okada T, Yamamoto A, et al. Grading glial tumors with amide proton transfer MR imaging: different analytical approaches. *J Neurooncol*. 2015;122:339–348.

323. Choi YS, Ahn SS, Lee S-K, et al. Amide proton transfer imaging to discriminate between low- and high-grade gliomas: added value to apparent diffusion coefficient and relative cerebral blood volume. *Eur Radiol*. 2017;27:3181–3189.

324. Paech D, Windschuh J, Oberhollenzer J, et al. Assessing the predictability of IDH mutation and MGMT methylation status in glioma patients using relaxation-compensated multipool CEST MRI at 7.0 T. *Neuro Oncol*. 2018;20:1661–1671.

325. Dreher C, Oberhollenzer J, Meissner J-E, et al. Chemical exchange saturation transfer (CEST) signal intensity at 7 T MRI of WHO IV° gliomas is dependent on the anatomic location. *J Magn Reson Imaging*. 2019;49:777–785.

326. Jiang S, Zou T, Eberhart CG, et al. Predicting IDH mutation status in grade II gliomas using amide proton transfer-weighted (APTw) MRI. *Magn Reson Med*. 2017;78:1100–1109.

327. Heo HY, Jones CK, Hua J, et al. Whole-brain amide proton transfer (APT) and nuclear Overhauser enhancement (NOE) imaging in glioma patients using low-power steady-state pulsed chemical exchange saturation transfer (CEST) imaging at 7T. *J Magn Reson Imaging*. 2016;44:41–50.

328. Paech D, Zaiss M, Meissner J-E, et al. Nuclear Overhauser enhancement mediated chemical exchange saturation transfer imaging at 7 Tesla in glioblastoma patients. *PLoS One*. 2014;9:e104181.

329. Paech D, Burth S, Windschuh J, et al. Nuclear Overhauser enhancement imaging of glioblastoma at 7 Tesla: region specific correlation with apparent diffusion coefficient and histology. *PLoS One*. 2015;10:e0121220.

330. Msayib Y, Harston GWJ, Tee YK, et al. Quantitative CEST imaging of amide proton transfer in acute ischaemic stroke. *Neuroimage Clin*. 2019;23:101833.

331. Gerigk L, Schmitt B, Stieltjes B, et al. 7 Tesla imaging of cerebral radiation necrosis after arteriovenous malformations treatment using amide proton transfer (APT) imaging. *J Magn Reson Imaging*. 2012;35:1207–1209.

332. Davis KA, Nanga RPR, Das S, et al. Glutamate imaging (GluCEST) lateralizes epileptic foci in nonlesional temporal lobe epilepsy. *Sci Transl Med*. 2015;7:309ra161.

333. Neal A, Moffat BA, Stein JM, et al. Glutamate weighted imaging contrast in gliomas with 7 Tesla magnetic resonance imaging. *Neuroimage Clin*. 2019;22:101694.

334. Zimmermann F, Korzowski A, Breitling J, et al. A novel normalization for amide proton transfer CEST MRI to correct for fat signal-induced artifacts: application to human breast cancer imaging. *Magn Reson Med*. 2020;83:920–934.

335. Loi L, Zimmermann F, Goerke S, et al. Relaxation-compensated CEST (chemical exchange saturation transfer) imaging in breast cancer diagnostics at 7T. *Eur J Radiol*. 2020;129:109068.

336. Zaric O, Farr A, Rodriguez EP, et al. 7 T CEST MRI: a potential imaging tool for the assessment of tumor grade and cell proliferation in breast cancer. *Magn Reson Imaging*. 2019;59:77–87.

337. Krikken E, Khlebnikov V, Zaiss M, et al. Amide chemical exchange saturation transfer at 7 T: a possible biomarker for detecting early response to neoadjuvant chemotherapy in breast cancer patients. *Breast Cancer Res*. 2018;20:51.

338. Krishnamoorthy G, Nanga RPR, Bagga P, et al. High quality three-dimensional gagCEST imaging of in vivo human knee cartilage at 7 Tesla. *Magn Reson Med*. 2017;77:1866–1873.

339. Trattnig S, Zbýň S, Schmitt B, et al. Advanced MR methods at ultra-high field (7 Tesla) for clinical musculoskeletal applications. *Eur Radiol*. 2012;22:2338–2346.

340. McMahon MT, Chan KW. Developing MR probes for molecular imaging. *Adv Cancer Res*. 2014;124:297–327.

341. Hancu I, Dixon WT, Woods M, et al. CEST and PARACEST MR contrast agents. *Acta Radiol*. 2010;51:910–923.

342. Paech D, Radbruch A. Dynamic glucose-enhanced MR imaging. *Magn Reson Imaging Clin N Am*. 2021;29:77–81.

343. Xu X, Yadav NN, Knutsson L, et al. Dynamic glucose-enhanced (DGE) MRI: translation to human scanning and first results in glioma patients. *Tomography*. 2015;1:105–114.

344. Schuenke P, Paech D, Koehler C, et al. Fast and quantitative T1ρ-weighted dynamic glucose enhanced MRI. *Sci Rep*. 2017;7:42093.

345. Schuenke P, Koehler C, Korzowski A, et al. Adiabatically prepared spin-lock approach for T1ρ-based dynamic glucose enhanced MRI at ultrahigh fields. *Magn Reson Med*. 2017;78:215–225.

346. Paech D, Schuenke P, Koehler C, et al. T1ρ-weighted dynamic glucose-enhanced MR imaging in the human brain. *Radiology*. 2017;285:914–922.

347. Tao J, Bistra I, Kevin HT, et al. Chemical exchange–sensitive spin-lock (CESL) MRI of glucose and analogs in brain tumors. *Magn Reson Med*. 2018;80:488–495.

348. Paech D, Radbruch A. CEST, pH, and glucose imaging as markers for hypoxia and malignant transformation. In: Pope WB, ed. *Glioma Imaging: Physiologic, Metabolic, and Molecular Approaches*. Cham, Switzerland: Springer; 2020:161–172.

349. Zaiss M, Herz K, Deshmane A, et al. Possible artifacts in dynamic CEST MRI due to motion and field alterations. *J Magn Reson*. 2019;298:16–22.
350. Boyd PS, Breitling J, Zimmermann F, et al. Dynamic glucose-enhanced (DGE) MRI in the human brain at 7 T with reduced motion-induced artifacts based on quantitative R1ρ mapping. *Magn Reson Med*. 2020;84:182–191.
351. Herz K, Lindig T, Deshmane A, et al. T1ρ-based dynamic glucose-enhanced (DGEρ) MRI at 3 T: method development and early clinical experience in the human brain. *Magn Reson Med*. 2019;82:1832–1847.
352. Xu X, Sehgal AA, Yadav NN, et al. d-glucose weighted chemical exchange saturation transfer (glucoCEST)-based dynamic glucose enhanced (DGE) MRI at 3T: early experience in healthy volunteers and brain tumor patients. *Magn Reson Med*. 2020;84:247–262.
353. Budinger TF, Bird MD. MRI and MRS of the human brain at magnetic fields of 14T to 20T: technical feasibility, safety, and neuroscience horizons. *Neuroimage*. 2018;168:509–531.
354. Budinger TF, Bird MD, Frydman L, et al. Toward 20 T magnetic resonance for human brain studies: opportunities for discovery and neuroscience rationale. *MAGMA*. 2016;29:617–639.
355. Wissenschaftsrat (German Council of Science and Humanities). 2017. Available at: www.wissenschaftsrat.de/download/archiv/6410-17. Accessed April 2021.
356. Parizh M, Lvovsky Y, Sumption M. Conductors for commercial MRI magnets beyond NbTi: requirements and challenges. *Supercond Sci Technol*. 2017; 30:014007.
357. Grant A, Metzger GJ, Van de Moortele PF, et al. 10.5 T MRI static field effects on human cognitive, vestibular, and physiological function. *Magn Reson Imaging*. 2020;73:163–176.
358. Houpt TA, Cassell J, Carella L, et al. Head tilt in rats during exposure to a high magnetic field. *Physiol Behav*. 2012;105:388–393.
359. Ward BK, Roberts DC, Otero-Millan J, et al. A decade of magnetic vestibular stimulation: from serendipity to physics to the clinic. *J Neurophysiol*. 2019; 121:2013–2019.
360. Tenforde TS. Magnetically induced electric fields and currents in the circulatory system. *Prog Biophys Mol Biol*. 2005;87:279–288.
361. Winter L, Seifert F, Zilberti L, et al. MRI-related heating of implants and devices: a review. *J Magn Reson Imaging*. 2021;53:1646–1665.
362. Guerin B, Angelone LM, Dougherty D, et al. Parallel transmission to reduce absorbed power around deep brain stimulation devices in MRI: impact of number and arrangement of transmit channels. *Magn Reson Med*. 2020;83: 299–311.